Article

The metastatic spread of breast cancer accelerates during sleep

https://doi.org/10.1038/s41586-022-04875-y

Received: 10 July 2021

Accepted: 16 May 2022

Published online: 22 June 2022

Check for updates

Zoi Diamantopoulou[1], Francesc Castro-Giner[1], Fabienne Dominique Schwab[2,3], Christiane Foerster[4,5], Massimo Saini[1], Selina Budinjas[1], Karin Strittmatter[1], Ilona Krol[1], Bettina Seifert[6], Viola Heinzelmann-Schwarz[3], Christian Kurzeder[3,4], Christoph Rochlitz[7], Marcus Vetter[6], Walter Paul Weber[4,5] & Nicola Aceto[1]✉

The metastatic spread of cancer is achieved by the haematogenous dissemination of circulating tumour cells (CTCs). Generally, however, the temporal dynamics that dictate the generation of metastasis-competent CTCs are largely uncharacterized, and it is often assumed that CTCs are constantly shed from growing tumours or are shed as a consequence of mechanical insults[1]. Here we observe a striking and unexpected pattern of CTC generation dynamics in both patients with breast cancer and mouse models, highlighting that most spontaneous CTC intravasation events occur during sleep. Further, we demonstrate that rest-phase CTCs are highly prone to metastasize, whereas CTCs generated during the active phase are devoid of metastatic ability. Mechanistically, single-cell RNA sequencing analysis of CTCs reveals a marked upregulation of mitotic genes exclusively during the rest phase in both patients and mouse models, enabling metastasis proficiency. Systemically, we find that key circadian rhythm hormones such as melatonin, testosterone and glucocorticoids dictate CTC generation dynamics, and as a consequence, that insulin directly promotes tumour cell proliferation in vivo, yet in a time-dependent manner. Thus, the spontaneous generation of CTCs with a high proclivity to metastasize does not occur continuously, but it is concentrated within the rest phase of the affected individual, providing a new rationale for time-controlled interrogation and treatment of metastasis-prone cancers.

CTCs are pioneers of the metastatic cascade in several cancer types, including breast cancer[1]. The factors that regulate spontaneous CTC intravasation in physiological settings are poorly understood, and the general assumption is that CTCs are constantly generated from invasive cancerous tissues[2], or generated following mechanical cues such as surgery[3] or physical activity[4]. In patients and in mouse cancer models, the exact timing of the events that characterize metastatic cancer progression, and the principles that dictate intravasation of CTCs and their proclivity to metastasize, are unclear. A better understanding of these processes may result in new approaches for cancer investigation and treatment.

Circadian rhythm and CTC intravasation

We first sought to determine CTC abundance and composition in hospitalized women with progressive breast cancer who had no treatment or were temporarily off-treatment and who consented to donate blood during the active (10:00 am) and rest (4:00 am) phases of the same day, including a total of 30 patients (Fig. 1a). Of these, 21 patients were diagnosed with early breast cancer (no metastasis) and 9 were diagnosed with stage IV metastatic disease at the time of blood sampling (Supplementary Table 1). Strikingly, following antigen-agnostic microfluidic capture of CTCs and confirmation through immunofluorescence staining[5], we found most CTCs (78.3%) in samples obtained at night time during the rest phase, including single CTCs, CTC clusters and CTC–white blood cell (WBC) clusters (Fig 1a, Extended Data Fig. 1a and Supplementary Table 1). To test the generality of these findings and to finely characterize the precise timing of the events, we used four different mouse models of breast cancer, including xenografts derived from human breast CTCs (NSG-CDX-BR16), xenografts with established human breast cancer cells (NSG-LM2) or mouse breast cancer cells (NSG-4T1), and an immunocompetent syngeneic breast cancer model (BALB/c-4T1). Following transplantation of breast cancer cells in the mammary fat pad and tumour growth, we examined spontaneous CTC generation over time by means of terminal blood sampling and microfluidic CTC capture. Consistently with patient data, we found most CTC events (99.2% in NSG-LM2, 97% in NSG-CDX-BR16, 93.8% in NSG-4T1, 87% in BALB/c-4T1) to be present in samples obtained through cardiac puncture during the mouse rest phase (corresponding to daylight time, given the inverted circadian rhythm of rodents compared to humans[6]; Fig. 1b,c and Extended Data Fig. 1a). More precisely, when carrying out a time kinetic analysis of a 24-h time period at intervals of 4 h,

[1]Department of Biology, Institute of Molecular Health Sciences, Swiss Federal Institute of Technology (ETH) Zurich, Zurich, Switzerland. [2]Department of Biomedicine, University of Basel, Basel, Switzerland. [3]Department of Gynecologic Oncology, University Hospital Basel, Basel, Switzerland. [4]Breast Care Center, University Hospital Basel, Basel, Switzerland. [5]Department of Breast, Abdomen and Pelvis, University Hospital Basel and University of Basel, Basel, Switzerland. [6]Department of Hematology and Oncology, Cantonal Hospital Basel-Land, Liestal, Switzerland. [7]Department of Medical Oncology, University Hospital Basel, Basel, Switzerland. ✉e-mail: nicola.aceto@biol.ethz.ch

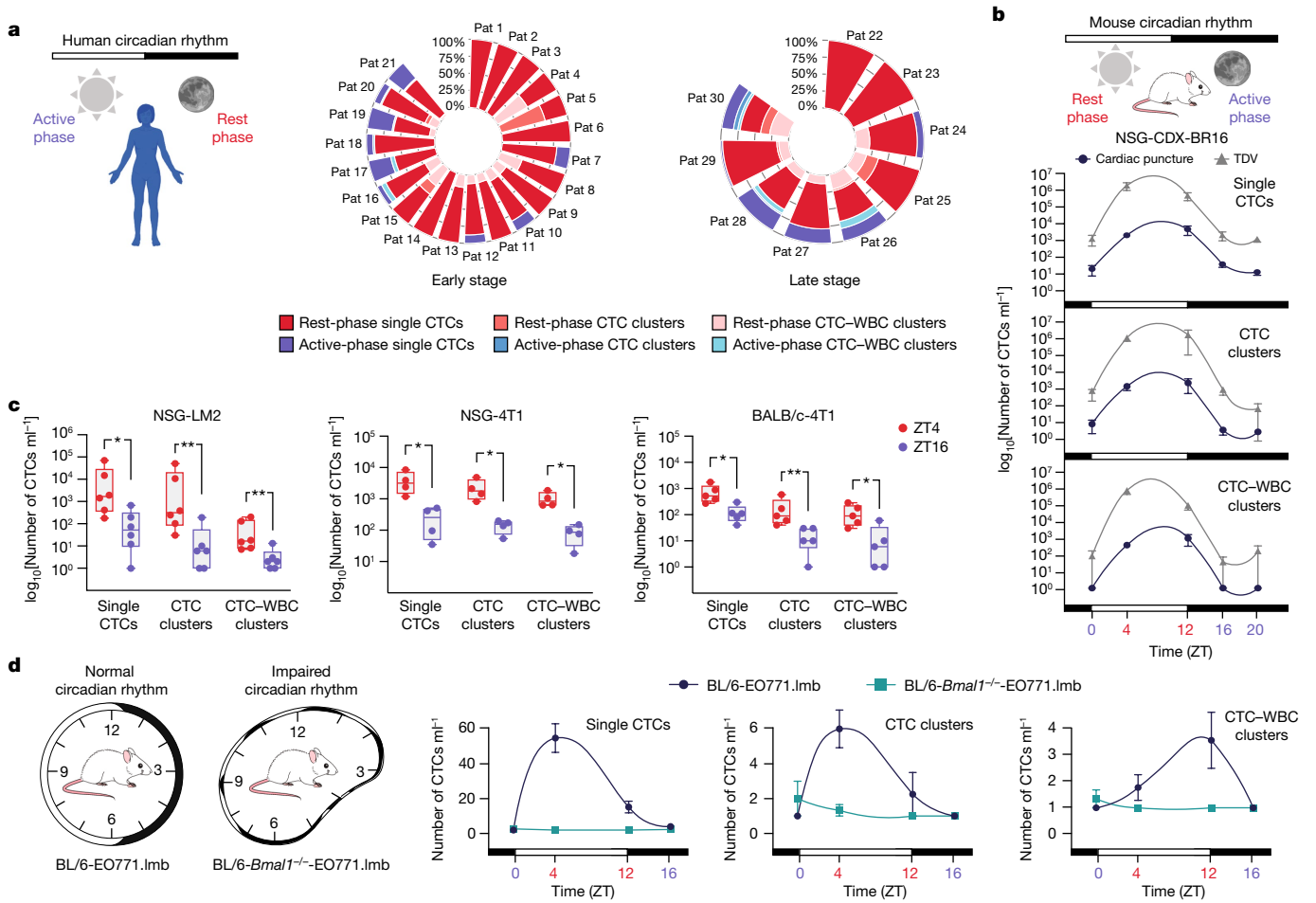

Fig. 1 | CTCs intravasate during the rest phase of the circadian rhythm. **a**, Left: graphical representation of the human circadian rhythm. The white and black bars represent environmental light (active period) and dark (rest period) conditions, respectively. Right: radial histograms showing the percentage of single CTCs, CTC clusters and CTC–WBC clusters isolated during the rest and active phases in patients with early- or late-stage breast cancer. $n = 21$ patients with early-stage cancer and $n = 9$ patients with late-stage cancer. Pat, patient. **b**, Top: graphical representation of the mouse circadian rhythm. The white and black bars represent environmental light (rest period) and dark (active period) conditions, respectively. Bottom: time kinetic analysis showing CTC counts in the NSG-CDX-BR16 mouse model of breast cancer, from blood collected through cardiac puncture or TDV over a 24-h time period ($n = 4$ for all time points, except ZT12 (cardiac puncture and TDV) and ZT20 (TDV), for which $n = 3$). **c**, Box plots showing the distribution of the number of CTCs collected at ZT4 and ZT16 in the immunocompromised NSG-LM2 ($n = 6$; single CTCs $P = 0.0152$; CTC clusters and CTC–WBC clusters $P = 0.0087$) and NSG-4T1 ($n = 4$; $P = 0.0286$ for all) and immunocompetent BALB/c-4T1 ($n = 5$; single CTCs $P = 0.0159$; CTC clusters $P = 0.0079$; CTC–WBC clusters $P = 0.0317$) mouse models of breast cancer. **d**, Left: graphical representation of physiological (BL/6-EO771.lmb mice) versus impaired circadian rhythm (BL/6-*Bmal1*$^{-/-}$-EO771.lmb mice). Right: graphs showing time kinetic analysis of CTC counts (single CTCs, CTC clusters and CTC–WBC clusters) in BL/6-EO771.lmb (ZT4, ZT12, ZT16 $n = 4$; ZT0 $n = 3$) and BL/6-*Bmal1*$^{-/-}$-EO771.lmb ($n = 3$) mice, from blood collected through cardiac puncture over a 24-h time period. The data in **b**,**d** are presented as mean ± s.e.m.; for **c**, the centre lines in the box represent the median, the box limits represent the first and third quartiles, and the extremes of the whisker lines represent the minimum and maximum observed values. $^{*}P < 0.05$, $^{**}P < 0.01$ by two-sided Mann–Whitney test. n represents the number of biologically independent mice. The human figure, sun and moon were created with BioRender.com.

we observed a very prominent oscillatory pattern of CTC release, peaking between 4 and 12 h zeitgeber time (ZT; with ZT0 defined as 06:00 am when the lights turn on, and ZT12 defined as 06:00 pm when the lights turn off) corresponding to their rest phase (Fig. 1b and Extended Data Fig. 1b) in mice with analogous tumour burden (Extended Data Fig. 1c,d). When focusing on the two most representative time points for the rest (ZT4) and active (ZT16) phases of the mouse circadian rhythm, we observe marked differences in absolute and normalized CTC counts in all tested models, with a 6- to 88-fold increase for single CTCs, a 12- to 278-fold increase for CTC clusters and an 8- to 34-fold increase for CTC–WBC clusters during ZT4 (Fig. 1c and Extended Data Fig. 1e–g), whereas no changes are observed in the ratio of the various CTC types (Extended Data Fig. 1h). Further, we identified highly similar (yet, even more pronounced) oscillatory patterns in CTC abundance when blood samples were obtained directly from the tumour draining vessel (TDV; Fig. 1b and Extended Data Fig. 2a–e). Given these results, the extremely short circulation half-life of CTCs[7,8], and their similar clearance rate during different time points of the rest and active phases (Extended Data Fig. 2f,g), we conclude that the main differences in CTC abundance observed during the rest versus the active phase are to be ascribed to differences in intravasation rates. We then attempted to perturb the physiological rhythm of tumour-bearing mice by different means. First, on the one hand, we used well-established methods to shift the normal light/dark (LD) cycle, provoking a jet-lag effect[9], and on the other hand, we treated control and jet-lagged mice with melatonin, a key hormone that regulates the sleep cycle (Extended Data Fig. 3a). Strikingly, when analysing blood in all mice at ZT4, we find that jet-lag induction leads to a 38- to 282-fold decrease in single CTCs, a 63- to 484-fold decrease in CTC clusters and a 28- to 219-fold decrease in CTC–WBC clusters compared to those in control mice and with no changes in primary tumour

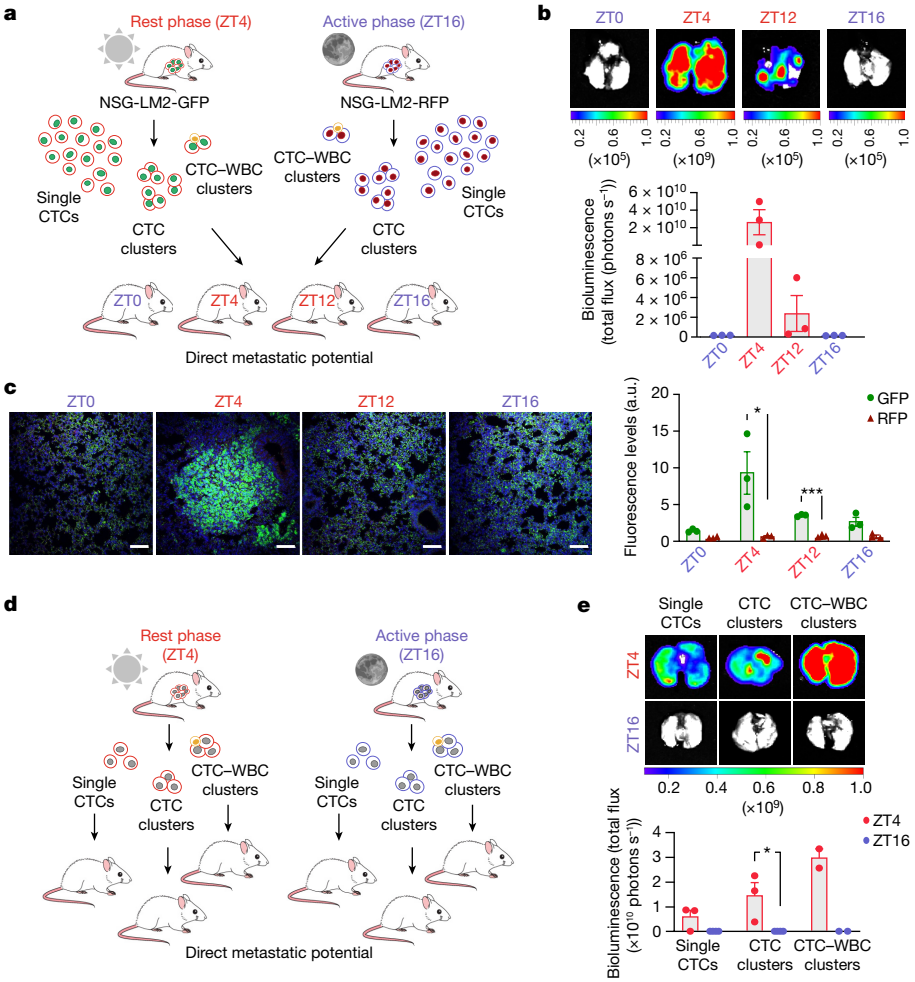

Fig. 2 | The metastatic potential of CTCs is highest during the rest phase. **a**, Schematic illustration of the experimental design for **b**,**c**, Equal numbers of spontaneously shed ZT4-generated GFP-labelled CTCs and ZT16-generated RFP-labelled CTCs from NSG-LM2 mice were co-injected through the tail vein into tumour-free recipient mice at different time points of the circadian rhythm (ZT0, ZT4, ZT12, ZT16) to measure their direct metastatic ability. **b**, Top: representative bioluminescence images of lungs from mice being co-injected simultaneously with ZT4-generated GFP-labelled CTCs and ZT16-generated RFP-labelled CTCs from NSG-LM2 mice. Bottom, plot showing normalized bioluminescence signal obtained from lungs of mice used in the same panel ($n = 3$). **c**, Left: representative immunofluorescence images of GFP (green) and RFP (red) in lungs of mice shown in **b**. Nuclei are stained with 4′,6-diamidino-2-phenylindole (DAPI; blue). Right: plot showing GFP and RFP levels in lungs of mice used in the same panel ($n = 3$; ZT4 $P = 0.0406$; ZT12 $P < 0.0001$). a.u., arbitrary units. Scale bars, 100 µm. **d**, Schematic illustration of the experimental design for **e**. Single CTCs, CTC clusters and CTC–WBC clusters are collected at ZT4 and ZT16 and separately injected into the tail vein of recipient tumour-free mice to measure their direct metastatic potential. **e**, Top: representative bioluminescence images of lungs from mice injected with single CTCs, CTC clusters or CTC–WBC clusters collected at ZT4 and ZT16 from NSG-LM2 mice. Bottom: plot showing normalized bioluminescence signal obtained from lungs of mice used in the same panel ($n = 3$ for ZT4 single CTCs and CTC clusters; $n = 4$ for ZT16 single CTCs and CTC clusters; $n = 2$ for CTC–WBC clusters, owing to their rarity; $P = 0.0272$ for CTC clusters at ZT4 versus ZT16). For all panels, the data are presented as mean ± s.e.m.; $^{*}P < 0.05$, $^{***}P < 0.001$ by unpaired two-sided *t*-test. *n* represents the number of biologically independent mice. The sun and moon were created with BioRender.com.

size (Extended Data Fig. 3b–d). Further, when treating tumour-bearing mice with melatonin (daily, 2 h before the start of the rest phase), and exposing them to a jet-lagged or normal LD cycle for a total duration of 22 days, we find a marked melatonin-induced increase in the production of single CTCs, CTC clusters and CTC–WBC clusters in all cases, rescued by the melatonin receptor antagonist luzindole (Extended Data Fig. 3e). Along with the effects of melatonin in increasing CTC production and luzindole in decreasing it without affecting primary tumour size, we observe an augmented or reduced metastatic burden, respectively (Extended Data Fig. 3f,g). We then exposed tumour-bearing mice to altered LD cycles. We used a long-day photoperiod (14:10 LD), as well as two different T-cycles with LD cycles that differ from 24 h (20-t, 10:10 LD and 28-t, 14:14 LD), and tested their effect on CTC generation. We observe a consistent increase in CTC counts during the rest phase in each of these light conditions (Extended Data Fig. 4a–d), suggesting a key role for light exposure, and its consequences, in CTC intravasation. Last, given the oscillatory pattern of CTC intravasation and its relation to the circadian rhythm, we tested whether this pattern was abolished in the context of a syngeneic transplantation of E0771.lmb mouse cancer cells in either wild-type BL/6 mice (BL/6-E0771.lmb) or in *Bmal1*-homozygous-knockout mice (BL/6-*Bmal1*$^{-/-}$-E0771.lmb), the only arrhythmic single-gene-knockout model[10] (Fig. 1d). We find that, whereas CTC counts from both cardiac puncture and the TDV follow a typical oscillatory pattern in control BL/6-E0771.lmb mice, oscillation in CTC counts is lost in BL/6-*Bmal1*$^{-/-}$-E0771.lmb mice (Fig. 1d and Extended Data Fig. 4e). Of note, BL/6-*Bmal1*$^{-/-}$-E0771.lmb mice generally fail to generate CTCs despite identical tumour size and timing of sample collection compared to those for BL/6-E0771.lmb control mice (Extended Data Fig. 4f,g), highlighting that a disruption of the master regulator of the circadian clock results in abolished CTC intravasation.

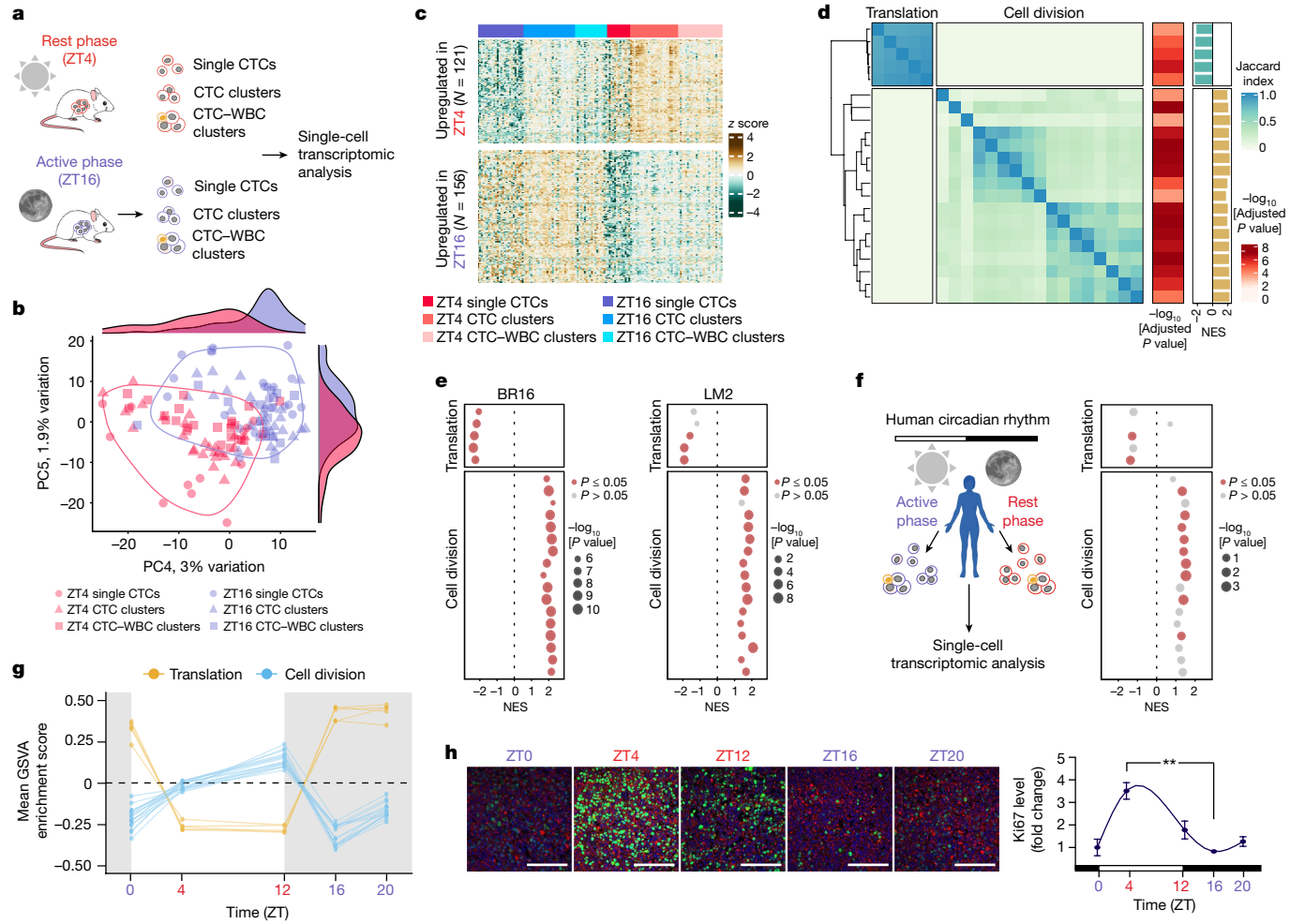

Fig. 3 | Rest-phase CTCs are highly proliferative. a, Illustration of the experimental design. CTCs are collected at ZT4 or ZT16, and then directly processed for scRNA-seq. **b**, Plot showing the principal components PC4 and PC5 of gene expression in CTCs from NSG-CDX-BR16 mice. The upper and right panels show the density of values for the active (blue) and rest (red) phases. **c**, Heatmap showing row-normalized abundance of differentially expressed genes between the rest and active phases in CTCs from NSG-BR16-CDX mice. *N* represents the number of upregulated genes. **d**, Heatmap showing the pairwise similarity of enriched gene sets in CTCs of the rest and active phases from NSG-CDX-BR16 mice. The heatmaps on the right represent the adjusted GSEA *P* value and normalized enrichment score (NES). **e**, Plots comparing the GSEA results (NES and *P* value) in the NSG-CDX-BR16 (left) and NSG-LM2 (right) models for gene sets shown in **d**. **f**, Left: illustration of the experimental design. CTCs were collected from patients with breast cancer during the rest (04:00 am) and active (10:00 am) phases, and then directly processed for scRNA-seq. The bar on the top represents environmental light (white) and dark (black) phases. Right: GSEA results in patient CTCs as described in **e**. **g**, Average gene set variation analysis (GSVA) score for translation (yellow, $n = 5$) and cell division (blue, $n = 17$) gene sets in CTCs from the NSG-LM2 time kinetic experiment (ZT0 $n = 3$, ZT4 $n = 3$, ZT12 $n = 3$, ZT16 $n = 3$, ZT20 $n = 3$). The background represents environmental light (white) and dark (grey) conditions. **h**, Left: representative immunofluorescence images of Ki67 (green) and Pan-CK (red) in primary tumours from NSG-LM2 mice dissected at ZT0, ZT4, ZT12, ZT16, ZT20 ($n = 3$; $P = 0.002$). Nuclei are stained with DAPI (blue). Scale bars, 100 µm. Right: plot showing the intensity of Ki67 in tumours of NSG-LM2 mice during different time points. The data are presented as mean ± s.e.m.; $^{**}P < 0.01$ by unpaired two-sided *t*-test. *n* represents the number of biologically independent mice. The human figure, sun and moon were created with BioRender.com.

Taken together, these results demonstrate that CTCs are not shed continuously during tumour progression, but the greatest release of single and clustered CTCs is achieved during sleep in both patients with breast cancer and mouse models.

Metastatic ability of CTCs during sleep

We next investigated whether, in addition to their increased production during the rest phase, CTCs that are generated during different phases of the circadian rhythm also harbour a different potential to successfully metastasize. To this end, we used the NSG-LM2 xenograft model, exclusively labelled with either GFP or RFP, and following tumour development, we isolated spontaneously shed CTCs at ZT4 (GFP-labelled) and ZT16 (RFP-labelled) by microfluidics-based capture. With a robotic micromanipulator, we isolated 150 ZT4-generated GFP-labelled CTCs and 150 ZT16-generated RFP-labelled CTCs, simultaneously, each of which composed of 110 single CTCs, 35 CTC clusters and 5 CTC–WBC clusters (representing typical CTC ratios in the NSG-LM2 model), and co-injected them through the tail vein of tumour-free recipient mice at different time points of the circadian rhythm (ZT0, ZT4, ZT12, ZT16) to measure their direct metastatic ability (Fig. 2a). Through in vivo bioluminescence imaging, we find the highest metastatic burden during the rest phase, and in particular at ZT4 (Fig. 2b). To dissect whether these metastases were derived from ZT4 or ZT16 CTCs, we conducted immunohistochemical analysis of the lungs with anti-GFP and anti-RFP antibodies. Remarkably, we find that most metastases derive from ZT4-generated GFP-labelled CTCs (Fig. 2c). These results highlight a substantial contribution of ZT4 CTCs to metastasis formation, as well as a higher proclivity of ZT4 CTCs to form metastases when injected into mice during their rest phase. Next we sought to extend our findings to further models

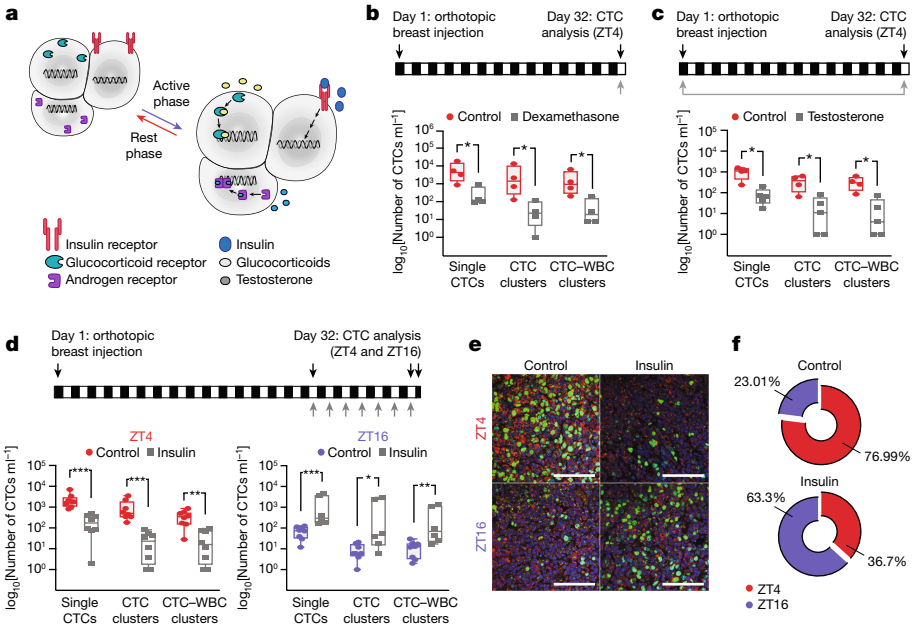

Fig. 4 | Dexamethasone, testosterone and insulin regulate CTC intravasation. a, Schematic illustration of the expression of three key receptors (insulin receptor, glucocorticoid receptor and androgen receptor) on breast cancer cells, activated by their circadian-rhythm-regulated ligands (insulin, glucocorticoid and testosterone, respectively) during the active phase. **b**, Box plots showing the distribution of the number of single CTCs, CTC clusters and CTC–WBC clusters isolated from mice treated with dexamethasone (4 mg kg^{-1}) or vehicle (0.03% dimethylsulfoxide; control) at ZT4 ($n = 4$; $P = 0.0286$ for all). **c**, Box plots showing the distribution of the number of single CTCs ($P = 0.0159$), CTC clusters ($P = 0.0317$) and CTC–WBC clusters ($P = 0.0159$) isolated from testosterone-treated ($n = 5$) or untreated (control) mice ($n = 4$) at ZT4. **d**, Box plots showing the distribution of the number of single CTCs (ZT4 $P = 0.0002$; ZT16 $P = 0.0007$), CTC clusters (ZT4 $P = 0.0002$; ZT16 $P = 0.0153$) and CTC–WBC clusters (ZT4 $P = 0.0011$; ZT16 $P = 0.0053$) isolated from mice treated with insulin (0.7 U kg^{-1}) or vehicle (phosphate-buffered saline; control) at ZT4 or ZT16 ($n = 8$, except insulin-treated mice at ZT16 with $n = 6$). **e**, Representative immunofluorescence images of Ki67 (green) and Pan-CK (red) in primary tumours from control or insulin-treated mice, dissected at ZT4 or ZT16 ($n = 4$ except control mice at ZT4 with $n = 3$). Nuclei are stained with DAPI (blue). Scale bars, 100 µm. **f**, Pie charts showing the mean percentage of Ki67 intensity in tumours shown in **e**. The NSG-LM2 model was used for all treatments. For **b**–**d**, the white and black bars on the horizontal axis represent environmental light and dark conditions, respectively; the grey arrows indicate treatment timing; the centre lines in the box represent the median; the box limits represent the first and third quartiles; the extremes of the whisker lines represent the minimum and maximum observed values. $^*P < 0.05$, $^{**}P < 0.01$, $^{***}P < 0.001$ by two-sided Mann–Whitney test. *n* represents the number of biologically independent mice.

and to precisely quantify the metastatic ability of rest-phase versus active-phase single CTCs, CTC clusters and CTC–WBC clusters, individually. We used both the NSG-CDX-BR16 and NSG-LM2 xenograft models, and following tumour development, we isolated spontaneously shed CTCs by microfluidics-based capture. With a robotic micromanipulator, we then isolated 100 single CTCs, 100 CTCs from CTC clusters and 100 CTCs from CTC–WBC clusters of mice during their rest (ZT4) and active (ZT16) phases, respectively, and injected them through the tail vein of tumour-free recipient mice at ZT12 to measure their direct metastatic ability (Fig. 2d). By means of bioluminescence imaging, we confirm that CTCs obtained during ZT4 exhibit an extraordinary metastasis-forming capacity compared to CTCs that are obtained during ZT16 (Fig. 2e and Extended Data Fig. 5a–f). Of note, when isolated during the rest phase and compared to those in the active phase, CTC clusters and CTC–WBC clusters seem to be endowed with greater metastasis-forming properties than those of single CTCs (Fig. 2e and Extended Data Fig. 5a–f), suggesting that most of the rest-phase-dependent metastatic spread of breast cancer could be ascribed to both homotypic and heterotypic CTC clusters. Together, these results indicate not only that CTC intravasation rates are increased, but also that their metastatic ability is augmented during the rest phase.

Time-dependent gene expression in CTCs

Next we sought to investigate molecular features determining the differential ability of CTCs to seed metastasis during the rest and active phases, respectively. Following mammary fat pad engraftment of BR16 and LM2 breast cancer cells, tumour growth and spontaneous CTC generation, we isolated single CTCs, CTC clusters and CTC–WBC clusters during the rest (ZT4) and active (ZT16) phases of the mouse circadian rhythm, and subjected them individually to single-cell RNA sequencing[11,12] (scRNA-seq; Fig. 3a). In total, after filtering for high-quality samples (that is, taking into account the number of expressed genes per cell, the total number of reads per cell and the proportion of reads aligning to mitochondrial genes; see Methods), we obtained a total of 138 CTCs from the NSG-CDX-BR16 model and 108 CTCs from the NSG-LM2 model, representing all types of CTC at ZT4 and ZT16. Using principal component analysis, we find that time point (ZT4 versus ZT16) is a key feature driving variance of gene expression in CTCs (Fig. 3b and Extended Data Fig. 6a), suggesting time-point-driven gene expression changes. Differential gene expression of samples isolated during the rest (ZT4) versus the active (ZT16) phase reveals a set of 121 upregulated genes in ZT4 CTCs ($\log_2$[fold change] ≥ 0.5 and false discovery rate ≤ 0.05) and a set of 156 upregulated genes in ZT16 CTCs ($\log_2$[fold change] ≤ −0.5 and false discovery rate ≤ 0.05; Fig. 3c and Supplementary Table 2). Of note, we observe that most of the genes defining ZT4 and ZT16 expression signatures are consistently found highly upregulated (that is, fold change) in all types of CTC, yet statistical significance is highest in CTC clusters and CTC–WBC clusters (Extended Data Fig. 6b,c). This is consistent with a higher variability and higher dropout rate expected in single-cell samples. Gene set enrichment analysis (GSEA) of genes upregulated during ZT4 and ZT16 highlights a highly consistent activity of pathways that support mitosis and cell division during ZT4 (adjusted *P* value ≤ 0.0001), mirrored by pathways that support

ribosomal biogenesis and translation of genes during ZT16 (adjusted *P* value ≤ 0.0001; Fig. 3d,e, Extended Data Fig. 6d,e and Supplementary Table 3). These findings are consistent with prototypical gene expression timing in eukaryotic cells (that is, comprising recurring ribosome biogenesis and gene translation phases followed by the expression of cell cycle progression genes and the execution of cellular division within a 24-h time frame)[13]. Of note, in human CTCs isolated from patients with breast cancer during the active (10:00 am) and rest (4:00 am) phases of the same day, we confirm the same pattern of gene expression and pathway activity as observed in mouse models (Fig. 3f and Extended Data Fig. 6e). Gene expression changes ascribed to cell division and translation and inferred at time points ZT4 and ZT16, respectively, are also consistently observed across different time points during the rest and active phases (Fig. 3g and Extended Data Fig. 6f). Given the short half-life of CTCs, we reasoned that oscillatory changes in cellular proliferation could also be visible at the level of the primary tumour when analysed at different times. Accordingly, when staining for the proliferation marker Ki67 in tumours from the NSG-CDX-BR16 and the NSG-LM2 models, along with their CTCs, we find a marked upregulation of Ki67 during the rest phase (Fig. 3h and Extended Data Fig. 7) and consistent with the timing of highest CTC intravasation and expression of mitosis-related genes. Together, molecular gene expression analysis of CTCs from patients and mouse models, isolated during the rest and active phases, highlights very distinct gene expression patterns. During sleep, gene expression is dominated by cell division and mitosis genes, whereas during the active phase, we observe high ribosome biogenesis activity. This oscillatory proliferation timing is observed not only in CTCs but also in the primary tumour, suggesting this as a general phenomenon occurring in breast cancer cells during disease progression.

Regulators of CTC intravasation

Mechanistically, to identify the master regulators of circadian-rhythm-driven CTC generation and proliferation, we took several approaches. We first investigated whether the expression of prototypical circadian clock genes in cancer cells changed between the rest (ZT4) and active (ZT16) phase. Similarly to previous reports highlighting disruption of rhythmicity in the expression of circadian clock genes in cancer[14,15], we could not detect differential expression in CTCs or primary tumour cells (Extended Data Fig. 8a–c), whereas we could confirm rhythmicity in non-neoplastic tissues (Extended Data Fig. 8c). We next investigated whether oscillations in CTC counts could be explained by changes in interstitial fluid pressure, differential interplay with immune cells and damage due to different haemolysis rates during different phases of the circadian rhythm. Notably, we found no difference in YAP and TAZ expression levels or localization (as sensors of interstitial pressure), in the abundance of circulating or tumour-infiltrated immune cells, or in apoptotic levels of CTCs during the rest (ZT4) versus active (ZT16) phase (Extended Data Fig. 9a–f). Last, we interrogated our RNA-seq data from CTCs of xenografts and patients to determine the expression levels of receptors for well-known circadian-rhythm-regulated hormones, growth factors or molecules, reasoning that the daily oscillation of their systemic levels could affect cancer cells in a time-dependent fashion. We evaluated the expression of 63 receptors for circadian-rhythm-regulated candidates (Supplementary Table 4), looking for those with a high level of expression in most CTCs and independently of a specific time point (that is, stable expression over time and activity proportional to the levels of their ligand). With these criteria, we find that expression of the glucocorticoid receptor, androgen receptor and insulin receptor is highly represented among single CTCs, CTC clusters and CTC–WBC clusters (Extended Data Fig. 10a), suggesting the involvement of their ligands in time-point-driven CTC generation and proliferation (Fig. 4a). To test this hypothesis, we first treated tumour-bearing mice with either dexamethasone (specific glucocorticoid receptor ligand) or testosterone (the main androgen receptor ligand), both found at high levels in physiological conditions at the onset of the active phase[16,17] (that is, when CTC numbers are low). Accordingly, both a single treatment with dexamethasone at 4 mg kg^{-1} during the rest phase (ZT2) and implantation of a testosterone pellet (slow, continuous release) resulted in a marked reduction in single CTCs, CTC clusters and CTC–WBC clusters when sampled at the peak time during the rest phase (ZT4; Fig. 4b,c and Extended Data Fig. 10b–f). Of note, whereas treatment with dexamethasone or testosterone did not affect primary tumour size (Extended Data Fig. 10c,d), we observed a reduction in the metastatic burden of testosterone-treated mice (Extended Data Fig. 10e), consistent with a prolonged suppression of CTC generation alongside the continuous testosterone release from the pellet. Further, given the well-established link between insulin stimulation and subsequent cell growth and division[13,18], we investigated whether insulin oscillations (with insulin being higher during the active phase following glucose intake in physiological conditions[19]) could also influence the proliferation timing and intravasation of breast cancer cells (that is, whether insulin stimulation during the rest phase could invert the dynamics of CTC release and proliferation). To address this, following tumour development, we treated tumour-bearing mice daily (during the rest phase, at ZT3) for 1 week with 0.7 U kg^{-1} of insulin and 1 g kg^{-1} glucose, and quantified CTC abundance during the rest and active phases, respectively. Consistently, we find that insulin treatment during the rest phase decreases CTC intravasation at ZT4, and increases it at ZT16 (Fig. 4d), with no significant changes in primary tumour volume (Extended Data Fig. 10g,h). Of note, treatment with insulin during the rest phase also inverts the proliferation cycle of breast cancer cells (that is, it decreases proliferation during the rest phase and it increases it during the active phase; Fig. 4e). Together, our findings indicate that proliferation and intravasation of breast cancer cells are dictated by daily oscillations in key circadian-rhythm-regulated hormones, whose action influences breast cancer metastasis dynamics.

Discussion

Our data provide new insights into the processes that dictate the generation of metastasis-competent CTCs. Previous reports have suggested a role of the circadian rhythm in tumorigenesis, with most involving epidemiological studies and linking disruption of the circadian clock to accelerated onset of cancer[15,20,21]. Yet, dynamics that prospectively govern metastatic disease progression in this context remained poorly characterized. More recent studies using in vivo imaging technologies and interrogation of physiological models have highlighted various mechanisms adopted by cancer cells during the intravasation process[22–24]; however, a detailed understanding of the specific timing of CTC intravasation has been lacking. We find that, in both patients with breast cancer and mouse models, generation of CTCs is highly restricted to the rest phase, and that rest-phase CTCs are endowed with a much greater metastatic proclivity compared to active-phase CTCs. This augmented metastatic ability is conferred by high proliferation rates that occur in a time-dependent manner, and it is influenced by the action of circadian-rhythm-regulated hormones, suggesting the need for time-controlled approaches for the characterization and treatment of breast cancer. These could include the interrogation of clinical samples at highly controlled time points to minimize variability, as well as cancer treatment approaches that are tuned to be maximally effective during sleep.

Online content

Any methods, additional references, Nature Research reporting summaries, source data, extended data, supplementary information, acknowledgements, peer review information; details of author contributions and competing interests; and statements of data and code availability are available at https://doi.org/10.1038/s41586-022-04875-y.

1. Pantel, K. & Speicher, M. R. The biology of circulating tumor cells. *Oncogene* **35**, 1216–1224 (2016).
2. Alix-Panabières, C. & Pantel, K. Circulating tumor cells: liquid biopsy of cancer. *Clin. Chem.* **59**, 110–118 (2013).
3. Li, S. et al. Less micrometastatic risk related to circulating tumor cells after endoscopic breast cancer surgery compared to open surgery. *BMC Cancer* **19**, 1070 (2019).
4. Zhu, X. et al. In vivo flow cytometry reveals a circadian rhythm of circulating tumor cells. *Light Sci. Appl.* **10**, 110 (2021).
5. Szczerba, B. M. et al. Neutrophils escort circulating tumour cells to enable cell cycle progression. *Nature* **566**, 553–557 (2019).
6. Ripperger, J. A., Jud, C. & Albrecht, U. The daily rhythm of mice. *FEBS Lett.* **585**, 1384–1392 (2011).
7. Aceto, N. et al. Circulating tumor cell clusters are oligoclonal precursors of breast cancer metastasis. *Cell* **158**, 1110–1122 (2014).
8. Sasportas, L. S. & Gambhir, S. S. Imaging circulating tumor cells in freely moving awake small animals using a miniaturized intravital microscope. *PLoS ONE* **9**, e86759 (2014).
9. Papagiannakopoulos, T. et al. Circadian rhythm disruption promotes lung tumorigenesis. *Cell Metab.* **24**, 324–331 (2016).
10. Bunger, M. K. et al. Mop3 is an essential component of the master circadian pacemaker in mammals. *Cell* **103**, 1009–1017 (2000).
11. Macaulay, I. C. et al. Separation and parallel sequencing of the genomes and transcriptomes of single cells using G&T-seq. *Nat. Protoc.* **11**, 2081–2103 (2016).
12. Picelli, S. et al. Full-length RNA-seq from single cells using Smart-seq2. *Nat. Protoc.* **9**, 171–181 (2014).
13. Polymenis, M. & Aramayo, R. Translate to divide: control of the cell cycle by protein synthesis. *Microb. Cell* **2**, 94–104 (2015).
14. Masri, S. & Sassone-Corsi, P. The emerging link between cancer, metabolism, and circadian rhythms. *Nat. Med.* **24**, 1795–1803 (2018).
15. Kettner, N. M., Katchy, C. A. & Fu, L. Circadian gene variants in cancer. *Ann. Med.* **46**, 208–220 (2014).
16. Ikeda, Y., Kumagai, H., Skach, A., Sato, M. & Yanagisawa, M. Modulation of circadian glucocorticoid oscillation via adrenal opioid-CXCR7 signaling alters emotional behavior. *Cell* **155**, 1323–1336 (2013).
17. Lucas, L. A. & Eleftheriou, B. E. Circadian variation in concentrations of testosterone in the plasma of male mice: a difference between BALB/cBy and C57BL/6By inbred strains. *J. Endocrinol.* **87**, 37–46 (1980).
18. Hill, D. J. & Milner, R. D. Insulin as a growth factor. *Pediatr. Res.* **19**, 879–886 (1985).
19. Crosby, P. et al. Insulin/IGF-1 drives PERIOD synthesis to entrain circadian rhythms with feeding time. *Cell* **177**, 896–909 (2019).
20. Van Dycke, K. C. G. et al. Chronically alternating light cycles increase breast cancer risk in mice. *Curr. Biol.* **25**, 1932–1937 (2015).
21. Blakeman, V., Williams, J. L., Meng, Q.-J. & Streuli, C. H. Circadian clocks and breast cancer. *Breast Cancer Res.* **18**, 89 (2016).
22. Zomer, A. et al. In vivo imaging reveals extracellular vesicle-mediated phenocopying of metastatic behavior. *Cell* **161**, 1046–1057 (2015).
23. van Rheenen, J. & Scheele, C. L. G. J. Intravital microscopy to illuminate cell state plasticity during metastasis. *Curr. Opin. Cell Biol.* **72**, 28–35 (2021).
24. Kienast, Y. et al. Real-time imaging reveals the single steps of brain metastasis formation. *Nat. Med.* **16**, 116–122 (2010).

Methods

Patient samples

All patients gave their informed written consent to participate in the study that took place at the University Hospital Basel under the Clinical Research Protocol (number 2020-00014) approved by the Swiss authorities (EKNZ, Ethics Committee northwest/central Switzerland) and in compliance with the Declaration of Helsinki. All patients were hospitalized and were either temporarily off-treatment (patients with stage IV disease) or before operation (patients with stage I–III disease) at the time of blood sampling. A 7.5-ml sample of peripheral blood was collected from patients with breast cancer during the rest (04:00 am) and active (10:00 am) phases of the same day in EDTA vacutainers. The time point for each sample collection was strictly followed.

Cell culture

Human CTC-derived BR16 cells were generated as previously described[25] from a patient with hormone-receptor-positive breast cancer at the University Hospital Basel and propagated as suspension cultures in a humidified incubator at 37 °C with 5% O_2 and 5% CO_2. MDA-MB-231 LM2 human breast cancer cells (obtained from J. Massagué, Memorial Sloan Kettering Cancer Center), E0771.lmb mouse breast cancer cells (obtained from R. Anderson, Olivia Newton-John Cancer Research Institute) and 4T1 mouse breast cancer cells (ATCC) were grown in Dulbecco's modified Eagle medium (Gibco, 11330-057) supplemented with 10% fetal bovine serum (Gibco, 10500064) in a humidified incubator at 37 °C with 20% O2 and 5% CO_2. LM2, BR16 and 4T1 cells were transduced with lentiviruses carrying either GFP–luciferase or mCherry–luciferase. Cell lines did not belong to the list of commonly misidentified cell lines (International Cell Line Authentication Committee) and were confirmed negative for mycoplasma contamination. Authentication is not applicable for the human CTC-derived BR16 cell line, the MDA-MB-231 LM2 human breast cancer cell line, and the E0771.lmb mouse breast cancer cell line. 4T1 mouse breast cancer cells were authenticated by Multiplexion GmbH. Finally, for the in vivo mouse immunocompetent experiments, 4T1 and E0771.lmb cells were transduced with lentiviruses carrying CD90.1.

Mouse experiments

All mouse experiments were carried out according to institutional and cantonal guidelines (approved mouse protocol number 3053, cantonal veterinary office of Basel-City; and approved mouse protocol number 33688, cantonal veterinary office of Zurich). Experimental endpoints that were allowed in our approved licence included tumour-related factors such as a maximum tumour size of 2,800 mm^3 or severe ulceration, as well as appearance and behaviour features such as hunching, piloerection or decreased activity. These limits were not exceeded in any of the experiments. Sample size calculations were not predetermined, but the number of animals was chosen to comply with the 3R principles. All mice were randomized before the start of each experiment, but blinding was not carried out. NSG (NOD-scid-Il2rgnull; The Jackson Laboratory), BALB/c (Janvier Labs) and C57BL/6J (The Jackson Laboratory) female mice were kept in pathogen-free conditions, according to institutional guidelines. *Bmal1*-knockout mice (C57BL/6J background) were purchased and genotyped from the The Jackson Laboratory. Animals were kept in a standard light-cycle photoperiod (12 h light/12 h dark; 12:12 LD) with ZT0 defined as lights on (06.00 am) and ZT12 defined as lights off (06.00 pm). For the 20-t and 28-t cycle studies, animals were kept in 10:10 LD or 14:14 LD cycle conditions, respectively. Orthotopic breast cancer lesions were generated in 8-week-old NSG females following injection with either 1×10^6 LM2-mCherry–luciferase cells (NSG-LM2 model), 1×10^6 BR16-GFP–luciferase cells (NSG-CDX-BR16 model) or 0.5×10^6 4T1-GFP–luciferase cells (NSG-4T1 model) into the mammary fat pad. Similarly, 0.5×10^6 4T1-CD90.1 cells were orthotopically injected into the mammary fat pad of 8-week-old BALB/c female mice (BALB/c-4T1 model). Finally, 1×10^6 E0771.lmb-CD90.1 cells were orthotopically injected into the mammary fat pad of 8-week-old wild-type (BL/6-E0771.lmb model) or *Bmal1*-knockout (BL/6-*Bmal1*$^{-/-}$-E0771.lmb model) mice. In all cases, breast cancer cells were inoculated in 100 µl of 50% Cultrex PathClear Reduced Growth Factor Basement Membrane Extract (R&D Biosystems, 3533-010-02) in phosphate-buffered saline (PBS). Blood draw for CTC analysis, organ dissection and IVIS bioluminescence imaging were carried out during the rest and active phases after 4.5 weeks for NSG-LM2, 4 weeks for NSG-4T1 and BALB/c-4T1, 3 weeks for BL/6-E0771.lmb and BL/6-*Bmal1*$^{-/-}$-E0771.lmb and 5–6 months for NSG-CDX-BR16 mice. The time point for each sample collection was strictly followed. All mice were randomized before mouse experiments and blindly selected before injection. Maximal approved tumour volume was never exceeded.

Mouse treatments

A total of 1×10^6 LM2-mCherry–luciferase cells were orthotopically injected into the mammary fat pad of 8-week-old NSG female mice. Following tumour development, mice were treated with different circadian-regulated hormones on the basis of their pharmacokinetic profiles and the possibility of developing negative regulatory loops following prolonged treatment. For melatonin, treatments started 10 days after the tumour injection, when tumours started growing exponentially and CTCs were not yet detectable in peripheral blood. Mice were treated daily with melatonin (20 mg kg^{-1}; Sigma-Aldrich, M5250-1G) alone or in combination with luzindole (5 mg kg^{-1}; Sigma-Aldrich, L2407). Luzindole treatments were carried out 30 min before melatonin treatment, which was administrated 1.5 h before the onset of the rest phase (ZT0). Blood collection and CTC analysis were carried out at ZT0. For dexamethasone, mice were treated with dexamethasone (4 mg kg^{-1}; Sigma-Aldrich, D1159-500MG) once 2 h before the blood collection (ZT4) to avoid the activation of the negative regulatory loop of the hypothalamus–pituitary–adrenal axis[26]. For testosterone, mice were injected with testosterone implants (Belma Technologies, T-M/60) 4 days before the tumour injection. Implants were kept until the day of the blood collection (ZT4). For insulin, treatments started 25 days after the tumour cell injection to avoid an effect of insulin on tumour growth. Mice were treated daily with insulin (0.7 U kg^{-1}; Humalog) in parallel with glucose (1 g kg^{-1}; Sigma-Aldrich, G7021) at ZT3. Blood collection and CTC analysis were carried out at ZT4 and ZT16. All treatments were administered as intraperitoneal injections in a final volume of 100 µl.

Jet-lag experiment

A total of 1×10^6 LM2-mCherry–luciferase or 0.5×10^6 4T1-GFP–luciferase cells were orthotopically injected into the mammary fat pad of 8-week-old NSG female mice. Jet lag was initiated 1 week after the tumour injection by placing the animals in altered light-cycle conditions with an 8-h light advance every 2–3 days[9]. Melatonin treatments in jet-lagged mice were administered daily, 1.5 h before the onset of each jet-lagged rest phase. Blood collection and CTC analysis were carried out at the onset of the rest phase.

CTC capture

For patient samples, 7.5 ml of peripheral blood was processed for microfluidic-based CTC capture within 1 h from blood draw. Using the Parsortix Cell Separation System (ANGLE), CTCs were captured in Cell Separation cassettes (GEN3D6.5) and then stained with an antibody cocktail containing EpCAM–AF488 (Cell Signaling Technology, CST5198), HER2–AF488 (BioLegend, 324410), EGFR–FITC (GeneTex, GTX11400) and CD45–BV605 (BioLegend, 304042). For mouse experiments, 0.8 ml of blood was collected through cardiac puncture and processed immediately. For the immunocompromised models, samples were stained only for CD45, as cancer cells were identified on the basis of mCherry or GFP expression. For the immunocompetent models, anti-CD45 staining was carried out in parallel with staining for

CD90.1 (OX-7 clone, BioLegend, 202508) to identify WBCs and cancer cells, respectively. The number of captured CTCs, including single CTCs, CTC clusters and CTC–WBC clusters, was determined while cells were still in the cassette. CTCs were then released from the cassette in Dulbecco's PBS (Gibco,14190169) onto ultra-low-attachment plates (Corning, 3471-COR) for further downstream analysis.

Direct metastatic potential assay

A total of 1×10^6 LM2-mCherry–luciferase, LM2-GFP–luciferase or BR16-GFP–luciferase cells were orthotopically injected into the mammary fat pad of 8-week-old NSG female mice. Following tumour development, blood was collected through heart puncture at ZT4 or at ZT16, and run through the Parsortix system, and captured CTCs were released onto ultra-low-attachment plates. Using the CellCelector, an automated single-cell picking system (ALS), single CTCs, CTC clusters and CTC–WBC clusters were individually micromanipulated and then each category was injected into the tail vein of recipient NSG mice. Metastasis onset and growth rate in lungs were non-invasively monitored on a weekly schedule with the IVIS bioluminescence system. The experiment was terminated 4 months post injection of LM2-mCherry–luciferase and LM2-GFP–luciferase cells or 5 months post injection of BR16-GFP–luciferase CTCs.

Immunofluorescence staining and confocal analysis

Dissected organs and primary tumours were fixed in 4% paraformaldehyde at 4 °C overnight. After paraffin embedding, the Thermo Scientific Rotary Microtome Microm HM 355S was used to cut slices of 7 µm in thickness. Following a standard deparaffinization/antigen retrieval protocol, samples were stained for pan-CK (1:65; GeneTex, GTX27753), Ki67 (1:250; Abcam, ab15580), GFP (D5.1; 1:200; Cell Signaling Technology, 2956), mCherry (16D7; 1:300: Invitrogen, M11217) and DAPI (1 µg ml^{-1}; Sigma-Aldrich, D9542-1MG). CTCs were cytocentrifuged onto microscope slides and fixed in 4% paraformaldehyde. Post-fixation, cells were washed with PBS, permeabilized for 5 min in 0.5% TritonX-100/PBS and blocked with 5% BSA in 0.1% Triton/PBS for 1 h before Ki67 (1:250; Abcam, ab15580), TAZ (1:100; BD Biosciences, 560235), YAP (D8H1X; 1:1000; Cell Signaling Technology, 14074) or cleaved caspase 3 (5A1E; 1:100; Cell Signaling Technology, 9664) antibody was added. Immunofluorescence imaging was carried out on a Leica SP5 confocal microscope, and images were taken using the 60× oil lens. All images were analysed by the Fiji image processing software (2.1.0/1.53c).

Flow cytometry

Mouse tumours were minced into fragments and enzymatically digested for 15 min with 2 mg ml^{-1} type IV collagenase plus 50 U ml^{-1} bovine DNase. The digested tumours were mechanically dissociated in C tubes using a GentleMACS device (Miltenyi), and then subjected to red blood cell lysis using ACK Buffer (Lonza) and immediately stained. Whole mouse blood was pelleted and red blood cells were lysed using ACK Buffer and immediately stained. For immunostaining, cells were blocked in a 2% FCS solution containing 2 mM EDTA and FcR blocking reagent (Miltenyi). Mouse peripheral blood cells were stained with the following antibodies: Alexa Fluor 594 anti-mouse Ly-6G (1:500; 1A8 clone, BioLegend, 127602), Alexa Fluor 594 anti-mouse CSF-1R/CD115 (1:200; AFS98 clone, BioLegend, 135520), APC/Cyanine7 anti-CD11b antibody (1:500; M1/70 clone, BioLegend, 101226), Brilliant Violet 421 anti-mouse CD3 (1:200; 17A2 clone, BioLegend, 100228), PE anti-mouse NKp46/CD335 (1:100; 29A1.4 clone, BioLegend, 137647), Alexa Fluor 647 anti-mouse CD49b (1:200; DX5 clone, BioLegend, 103511), Alexa Fluor 488 anti-mouse CD8a (1:200; 53-6.7 clone, BioLegend, 100723), Brilliant Violet 510 anti-mouse CD4 (1:500; GK1.5 clone, BioLegend, 100449), PE anti-mouse CD223/LAG-3 (1:100; C9B7W clone, BioLegend, 125224). Dissociated tumour cells were stained with the above-mentioned antibodies plus CD90.1 (1:500; OX-7 clone, BioLegend, 202508) to distinguish CD90.1-labelled cancer cells from the infiltrating stroma. All samples were processed on an LSR Fortessa device (BD) and further analysed with FlowJo (Tree Star).

scRNA-seq

Using the CellCelector, single CTCs, CTC clusters and CTC–WBC clusters were collected and immediately transferred into individual tubes (Axygen, 321-032-501) containing 2.5 µl RLT Plus lysis buffer and 1 U SUPERase IN RNase inhibitor (Invitrogen, AM2694). Samples were immediately frozen and kept at −80 °C until further processing. Amplified cDNA was prepared according to the Smart-seq2 protocol. Libraries were prepared using Nextera XT (Illumina) and sequenced on an Illumina NextSeq500 instrument in 75-base-pair single-read mode. This yielded a median raw sequencing depth of 1.64 million reads per sample.

RNA-seq analysis

Sequencing reads were quality trimmed with Trim Galore! (v0.6.5, https://www.bioinformatics.babraham.ac.uk/projects/trim_galore/; parameters: –q 20 –length 20) and Cutadapt (v3.4). Quality assessment of RNA-seq data was carried out using FastQC (v0.11.4, https://www.bioinformatics.babraham.ac.uk/projects/fastqc) and FastQ Screen (v0.11.4, https://www.bioinformatics.babraham.ac.uk/projects/fastq_screen/) and visualized with MultiQC (v1.7). Trimmed reads were aligned to human (GRCh38) genome reference using STAR (v.2.7.3a; parameters: --twopassMode Basic --outSAMmapqUnique 60 --sjdbGTFfile) with splice junctions from the human GENCODE annotation (release 35). To eliminate residual contamination from mouse RNA, reads derived from xenograft models were also aligned to the mouse (GRCm38) genome reference using STAR (v.2.7.3a; parameters: --twopassMode Basic --outSAMmapqUnique 60 --sjdbGTFfile), with splice junctions from the mouse GENCODE annotation (release M25) and assigned to either human or mouse using Disambiguate (v1.0.0). Resulting BAM files were sorted by Samtools (v1.10), and the alignment quality was evaluated using RSeQC (v.2.6.4). The gene-level expression counts were computed with featureCounts (v.2.0.1; parameters: -t exon -g gene_id --minOverlap 10 -Q 10) using the human gene annotations from GENCODE (release 35). Genes present with at least 3 reads in 50% of the samples were kept for the analysis. Single-cell samples were retained for further analyses if they had at least 50,000 reads, at least 5,000 genes with non-zero expression and less than 50% of reads mapping to mitochondrial genes. For samples containing more than 1 cell (CTC clusters and CTC–WBC clusters), the minimum number of genes was set to 8,000. Read counts were normalized using the trimmed mean of *M*-values method implemented in the R/Bioconductor package edgeR (v3.34.1). Quality control and visualization of processed data were carried out with the help of the R/Bioconductor scater package (v1.20.1). After normalization, principal component analysis was conducted using gene expression (log_2-normalized counts) of the top 500 genes with the largest biological components according to the getTopHVGs function from the R/Bioconductor package scran (v1.20.1). Selected principal components were associated with technical and biological variables using Pearson correlation. The number of PCs selected was defined by the elbow method.

Differential expression and GSEA

Differential expression was computed with the quasi-likelihood approach from the edgeR R/Bioconductor package (v3.34.1) using robust dispersion estimates. Before differential expression analysis, genes detected in less than 50% of the samples, considering the size of the smallest group of replicates, were removed from the analysis (threshold 5 counts per million). *P* values were adjusted for multiple comparisons using the Benjamini–Hochberg method. GSEA was conducted with the fast GSEA method implemented in the R/Bioconductor package clusterProfiler (v4.0.5). As input for GSEA, we used a list of genes ranked by fold-change and two gene set collections from the Molecular Signatures Database (MsigDB, v7.4): C2 canonical pathways

and C5 GO biological process. Fast GSEA carries out a preliminary estimation of enrichment *P* values using a permutation test (1,000 permutations) and a secondary estimation of low *P* values using the multilevel algorithm with a 1×10^{-10} boundary. An adjusted *P*-value cut-off of 0.0001 was applied to define enriched gene sets. Only gene sets with a size between 10 and 500 genes were included in the analysis. The Jaccard coefficient was computed to measure the similarity between the enriched terms using the genes included in the GSEA leading-edge subset within each gene set. In NSG-LM2 and patients, the GSEA analysis was carried out using only the enriched terms from the NSG-CDX-BR16 model. GSVA was conducted with the R/Bioconductor GSVA package to obtain sample level enrichment scores for the same MSigDB collections evaluated in the GSEA analysis. Differences in enrichment score across the multiple time points were estimated using the moderated *F* statistic obtained through the empirical Bayes approach implemented in the R/Bioconductor package limma v3.48.3. Time points with fewer than three replicates were removed from this analysis.

Data analysis

Data analysis, statistical testing and visualization were conducted in Graphpad Prism (v.9.1.1), R (version 4.1.0; R Foundation for Statistical Computing) and Bioconductor (v.3.13). Illustrations were created with BioRender. The figure legends describe the statistical approach used for each analysis.

Reporting summary

Further information on research design is available in the Nature Research Reporting Summary linked to this paper.

Data availability

RNA-seq data have been deposited in the Gene Expression Omnibus (GEO, National Center for Biotechnology Information; accession number GSE180097). Processed transcriptomics data, large datasets and other files required for reproducibility are available from the Zenodo data repository (https://doi.org/10.5281/zenodo.6358987). The human reference genome (GRCh38), mouse reference genome (GRCm38), human gene annotation (release 35) and mouse gene annotation (release M25) files were downloaded from GENCODE (https://www.gencodegenes.org). Gene sets were downloaded from the Molecular Signatures Database (MsigDB, v7.4, http://www.gsea-msigdb.org/gsea/msigdb/collections.jsp). All data are available from the corresponding author upon reasonable request. Source data are provided with this paper.

Code availability

Code related to the data analysis of this study has been deposited to GitHub (https://github.com/TheAcetoLab/diamantopoulou-ctc-dynamics) and archived at Zenodo (https://doi.org/10.5281/zenodo.6484917). Descriptions of how to reproduce the analysis workflows (showing code and R package version numbers) and the figures presented in this paper are available at https://theacetolab.github.io/diamantopoulou-ctc-dynamics.

25. Yu, M. et al. Ex vivo culture of circulating breast tumor cells for individualized testing of drug susceptibility. *Science* **345**, 216–220 (2014).
26. Jones, M. T., Hillhouse, E. W. & Burden, J. L. Dynamics and mechanics of corticosteroid feedback at the hypothalamus and anterior pituitary gland. *J. Endocrinol.* **73**, 405–417 (1977).

Acknowledgements We thank all the patients who donated blood for our study, as well as involved clinicians and study nurses. We thank members and collaborators of the laboratory of N.A. for scientific feedback and discussions. We thank J. Massagué (Memorial Sloan Kettering Cancer Center) for donating LM2 breast cancer cells; R. Anderson (Olivia Newton-John Cancer Research Institute) for donating E0771.lmb mouse breast cancer cells; the Genomics Facility Basel (D-BSSE of the ETH Zurich) for generating libraries and carrying out next-generation sequencing; P. Lorentz (University of Basel) for microscopy support; A. Offinger (University of Basel) and her team as well as the EPIC team (ETH Zurich) for support with animal work; M. Sonderegger-Stalder and K. Degener (Cantonal Hospital Basel-Land) for support with clinical samples. Research in the laboratory of N.A. is supported by the European Research Council (101001652), the strategic focus area of Personalized Health and Related Technologies at ETH Zurich (PHRT-541), the Future and Emerging Technologies programme of the European Commission (801159-B2B), the Swiss National Science Foundation (PP00P3_190077), the Swiss Cancer League (KLS-4834-08-2019), the Basel Cancer League (KLbB-4763-02-2019), the two Cantons of Basel through the ETH Zürich (PMB-01-16), the University of Basel and the ETH Zürich. Z.D. is an H2020 Marie Skłodowska-Curie Actions (101028567) Fellow.

Author contributions Z.D. and N.A. designed the study, carried out the experiments and wrote the manuscript. F.C.-G. carried out the computational analysis. M.S. generated the 4T1-CD90.1 cells and carried out the immune cell analysis. S.B. carried out immunofluorescence staining. K.S. contributed to mouse experiments and processed mouse tissues. I.K. processed blood samples. F.D.S., C.F., B.S., M.V., C.R., W.P.W., C.K. and V.H.-S. provided patient samples. All authors have read, commented on and approved the manuscript in its final form.

Competing interests N.A. is a co-founder and member of the board of PAGE Therapeutics AG, Switzerland, listed as an inventor in patent applications related to CTCs, a paid consultant for the Swiss Re Group, the Bracco Group, Tethis S.p.A, Thermo Fisher and ANGLE plc, and a Novartis shareholder. C.R. is a co-founder of PAGE Therapeutics AG, Switzerland. All other authors declare no competing interests.

Additional information
Supplementary information The online version contains supplementary material available at https://doi.org/10.1038/s41586-022-04875-y.
Correspondence and requests for materials should be addressed to Nicola Aceto.
Peer review information *Nature* thanks John Hogenesch, Sunitha Nagrath and the other, anonymous, reviewer(s) for their contribution to the peer review of this work.
Reprints and permissions information is available at http://www.nature.com/reprints.

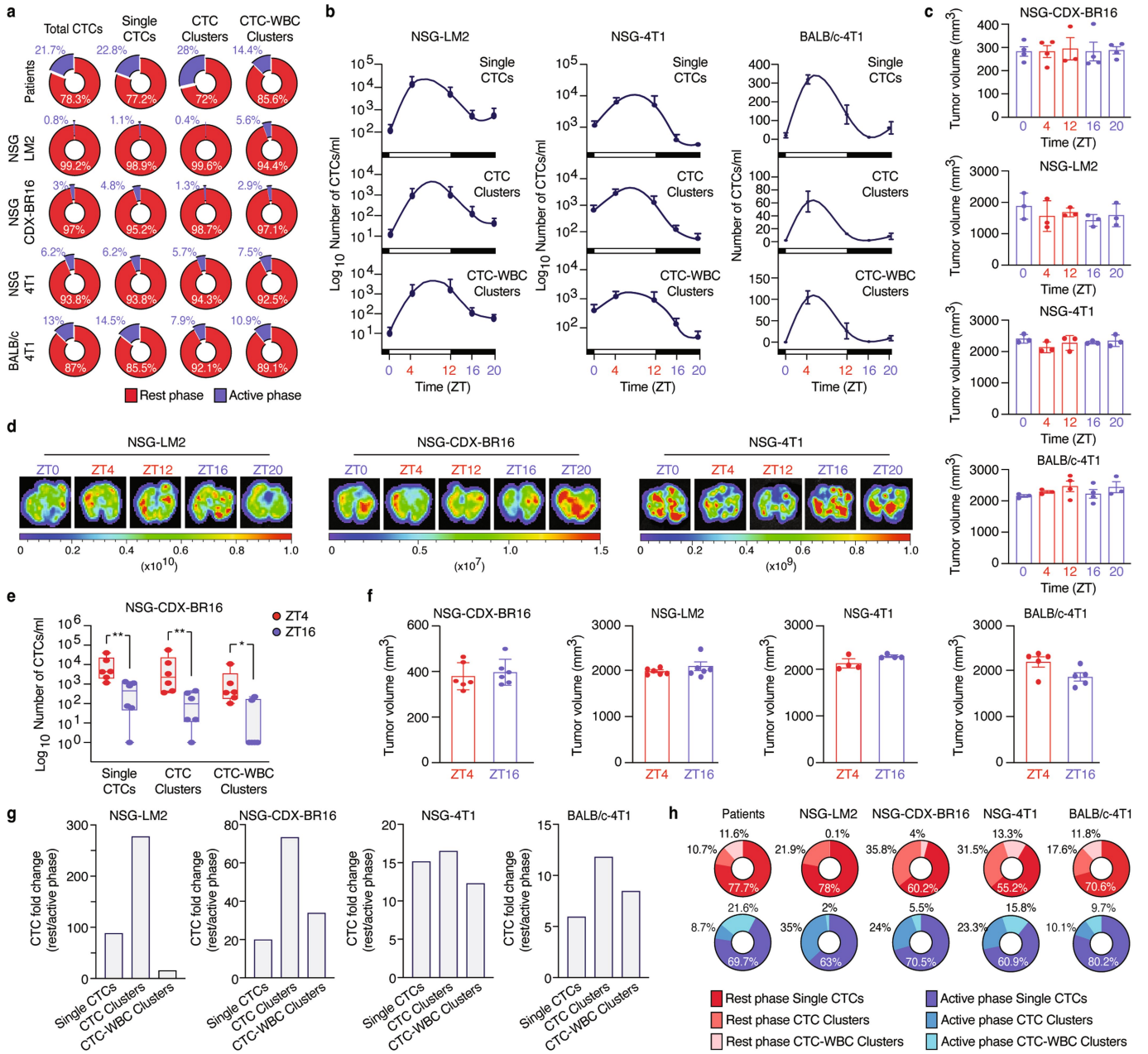

Extended Data Fig. 1 | Tumor size and CTCs intravasation rates during different phases of the circadian rhythm. a, Pie charts displaying the mean percent of total CTCs, single CTCs, CTC clusters and CTC-WBC clusters detected during the rest or active phase in breast cancer patients ($n = 30$), in NSG-LM2 mice ($n = 6$), NSG-CDX-BR16 mice ($n = 6$), NSG-4T1 mice ($n = 4$) or BALB/c-4T1 mice ($n = 6$). **b**, Time kinetic analysis showing mean CTC counts in the NSG-LM2 ($n = 3$), NSG-4T1 ($n = 3$) and BALB/c-4T1 (ZT0, ZT4, ZT20 $n = 3$; ZT12, ZT16 $n = 4$) breast cancer mouse models over a 24-h time period. Data are presented as mean ± s.e.m. **c**, Plots showing the size of the primary tumors dissected at different timepoints from NSG-CDX-BR16 mice (ZT0, ZT4, ZT16, ZT20 $n = 4$; ZT12 $n = 3$), NSG-LM2 ($n = 3$), NSG-4T1 mice ($n = 3$) and BALB/c-4T1 (ZT0, ZT4, ZT20 $n = 3$; ZT12, ZT16 $n = 4$) mice. Data are presented as mean ± s.e.m. **d**, Representative bioluminescence images of lungs from NSG-CDX-BR16, NSG-LM2 and NSG-4T1 mice taken at different timepoints (ZT0, ZT4, ZT12, ZT16, ZT20) ($n = 3$). **e**, Box plots showing the distribution of the number of single CTCs ($P = 0.0043$), CTC clusters ($P = 0.0087$) and CTC-WBC clusters ($P = 0.0130$) collected at ZT4 or ZT16 in the NSG-CDX-BR16 mouse model ($n = 6$). Center lines in the box represent the median; box limits represent first and third quartile; extremes of the whisker lines represent the minimum and maximum observed values. Data are presented as mean ± s.e.m.; $^{*}P < 0.05$, $^{**}P < 0.01$ by two-sided Mann-Whitney test. **f**, Plots showing the size of primary tumors from NSG-CDX-BR16 (n = 6), NSG-LM2 ($n = 6$), NSG-4T1 ($n = 4$) and BALB/c-4T1 ($n = 5$) mice dissected at ZT4 or ZT16. Data are presented as mean ± s.e.m. **g**, Plots showing the mean fold change increase of CTC counts isolated at ZT4 or ZT16 from NSG-LM2, NSG-CDX-BR16, NSG-4T1 and BALB/c-4T1 mice. **h**, Pie charts displaying the mean percentage of single CTCs, CTC clusters and CTC-WBC clusters detected during the rest or active phase in patients ($n = 7$), NSG-LM2 ($n = 6$), NSG-CDX-BR16 ($n = 6$), NSG-4T1 ($n = 4$) or BALB/c-4T1 ($n = 6$) mice. For all panels, n represents the number of biologically independent mice.

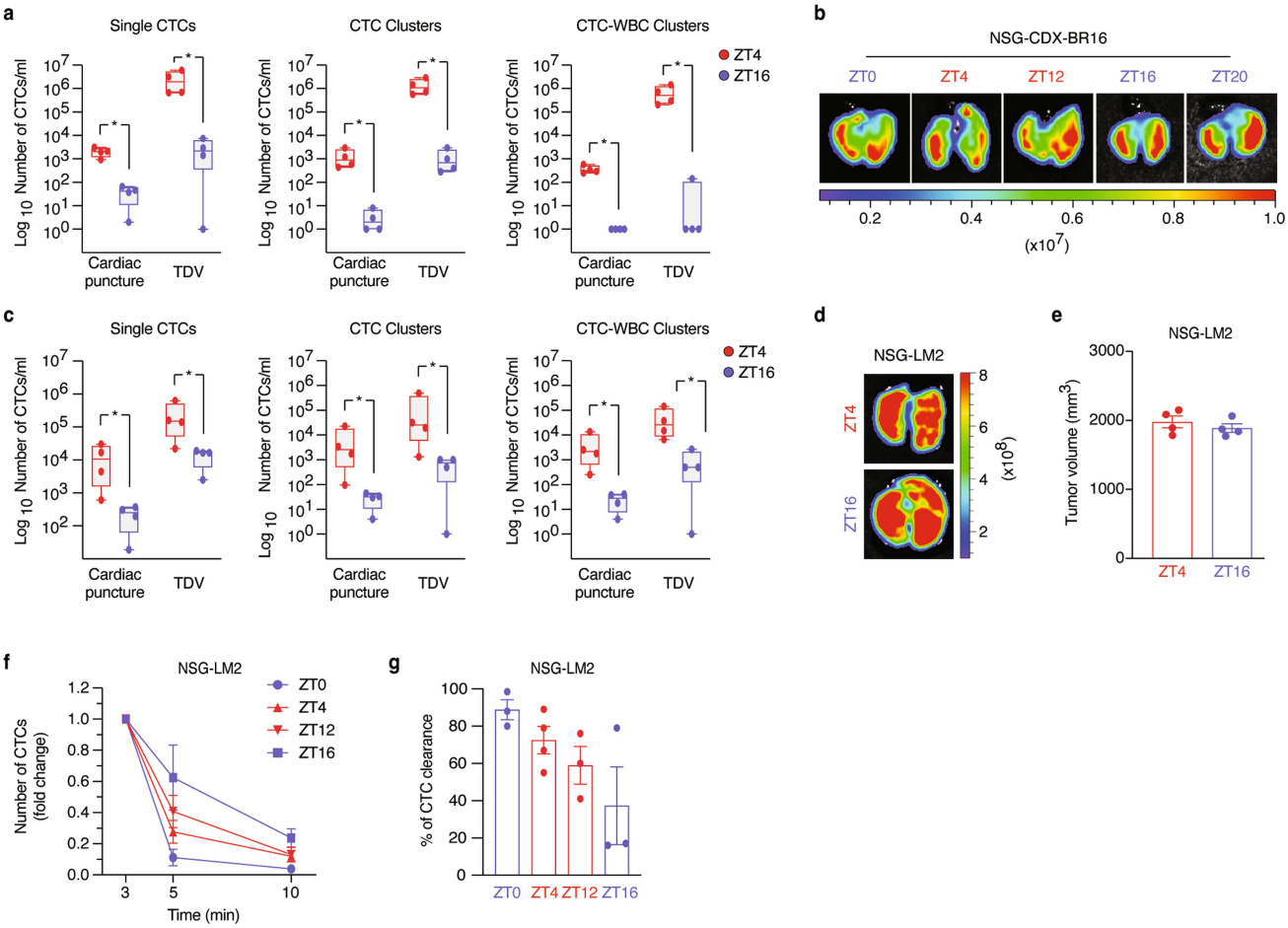

Extended Data Fig. 2 | The abundance of CTCs during the rest phase is due to increased intravasation. a, Box plots showing the distribution of the number of CTCs collected at ZT4 or ZT16 via cardiac puncture or tumor draining vessel (TDV) in the NSG-CDX-BR16 breast cancer mouse model ($n = 4$; $P = 0.0286$ for all). **b**, Representative bioluminescence images of lungs from NSG-CDX-BR16 mice taken at different timepoints (ZT0, ZT4, ZT12, ZT16, ZT20) over a 24-h time period ($n = 4$). **c**, Box plots showing the distribution of the number of CTCs collected at ZT4 or ZT16 via cardiac puncture or TDV in the NSG-LM2 breast cancer mouse model ($n = 4$; $P = 0.0286$ for all). **d**, Representative bioluminescence images of lungs from NSG-LM2 mice taken at ZT4 or ZT16 ($n = 4$). **e**, Plot showing the size of primary tumors dissected from NSG-LM2 mice at ZT4 or ZT16 ($n = 4$). **f**, Time kinetic analysis showing fold change differences in the number of LM2 cells detected in the circulation after their intravascular inoculation at different time points of the circadian rhythm (ZT0, ZT4, ZT12, ZT16) ($n = 3$ except ZT4 where $n = 4$). **g**, Plots showing the percentage of CTC clearance at different time points of the circadian rhythm (ZT0, ZT4, ZT12, ZT16) 5 min after intravascular inoculation of LM2 cells ($n = 3$ except ZT4 where $n = 4$). For panels "e", "f" and "g", data are presented as mean ± s.e.m. For panels 'a' and "c", center lines in the box represent the median; box limits represent first and third quartile; extremes of the whisker lines represent the minimum and maximum observed values. * $P < 0.05$ by two-sided Mann-Whitney test. For all panels, n represents the number of biologically independent mice.

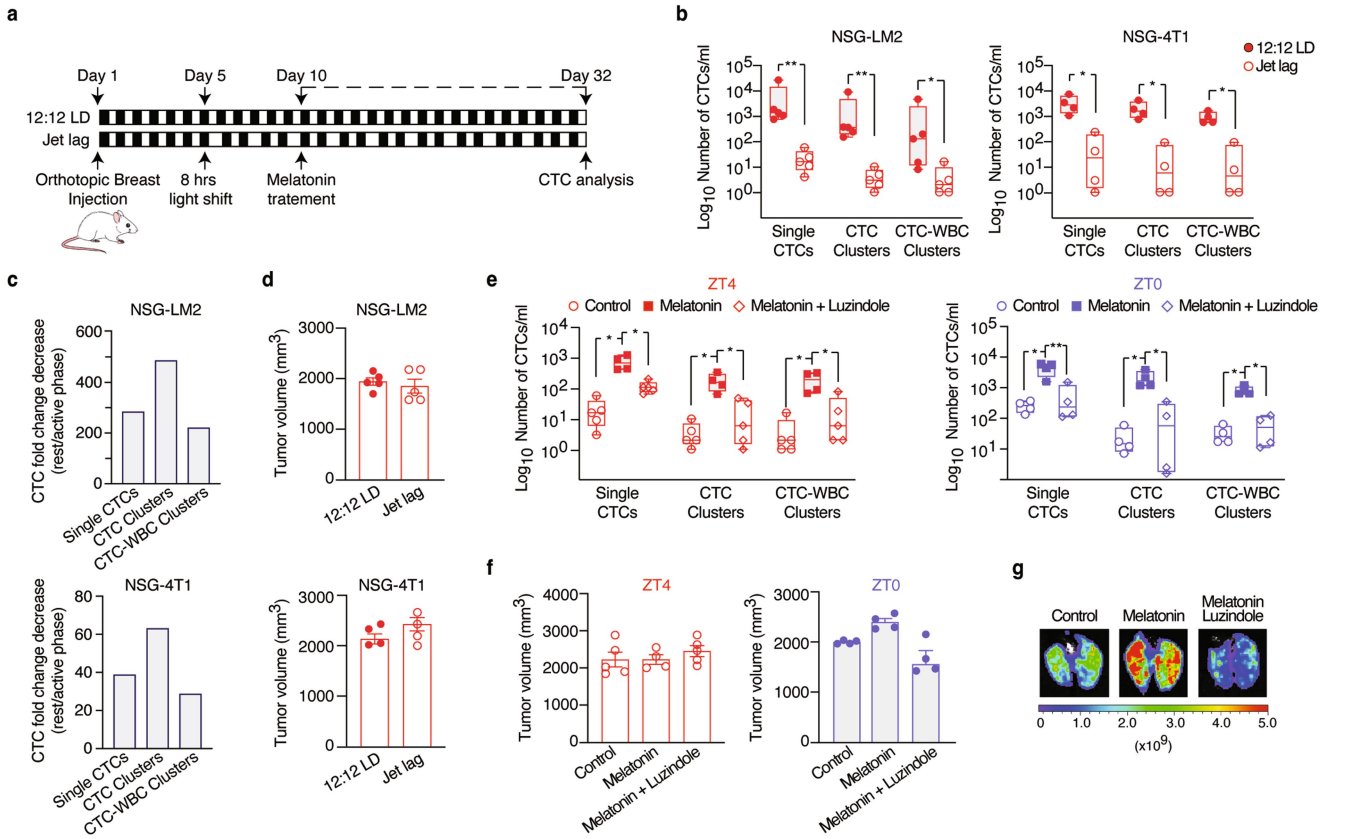

Extended Data Fig. 3 | Circadian rhythm and melatonin regulate the intravasation of CTCs. a, Illustration of the experimental design for "b" and "e". **b**, Box plots showing the mean number of CTCs isolated from NSG-LM2 ($n = 5$; single CTCs $P = 0.0079$, CTC clusters $P = 0.0079$, CTC-WBC clusters $P = 0.0317$) and NSG-4T1 ($n = 4$; $P = 0.0286$ for all) mice that were kept in standard light cycle conditions (12:12, LD) or being jet-lagged. The blood draw was performed at ZT4. **c**, Plots showing the mean fold change decrease of CTC counts upon jet lag in NSG-LM2 ($n = 5$) and NSG-4T1 ($n = 4$) mice shown in "b". **d**, Plots showing the size of primary tumors dissected from NSG-LM2 ($n = 5$) and NSG-4T1 ($n = 4$) mice shown in "b". Data are presented as mean ± s.e.m. **e**, Box plots showing the distribution of the number of CTCs isolated from NSG-LM2 mice that were being jet-lagged (*left*) or kept in standard light cycle conditions (*right*) and were treated with melatonin alone or in combination with its antagonist luzindole. The blood draw was performed at ZT4 or ZT0. ($n = 4$, except control and melatonin-treated mice in combination with luzindole at ZT4 where $n = 5$; ZT4 $P = 0.0159$ except CTC-WBC clusters treated with melatonin in combination with lunzindole where $P = 0.0317$; ZT0 $P = 0.0286$ except single CTCs treated with melatonin in combination with lunzindole where $P = 0.0091$). **f**, Plots showing the size of primary tumors dissected from mice shown in "e". Data are presented as mean ± s.e.m. **g**, Representative bioluminescence images of lungs from NSG-LM2 mice that were kept in standard light cycle conditions (12:12, LD) and were treated with melatonin alone or in combination with luzindole. For panels 'b' and "e", center lines in the box represent the median; box limits represent first and third quartile; extremes of the whisker lines represent the minimum and maximum observed values. * $P < 0.05$, ** $P < 0.01$ by two-sided Mann-Whitney test. For all panels, n represents the number of biologically independent mice.

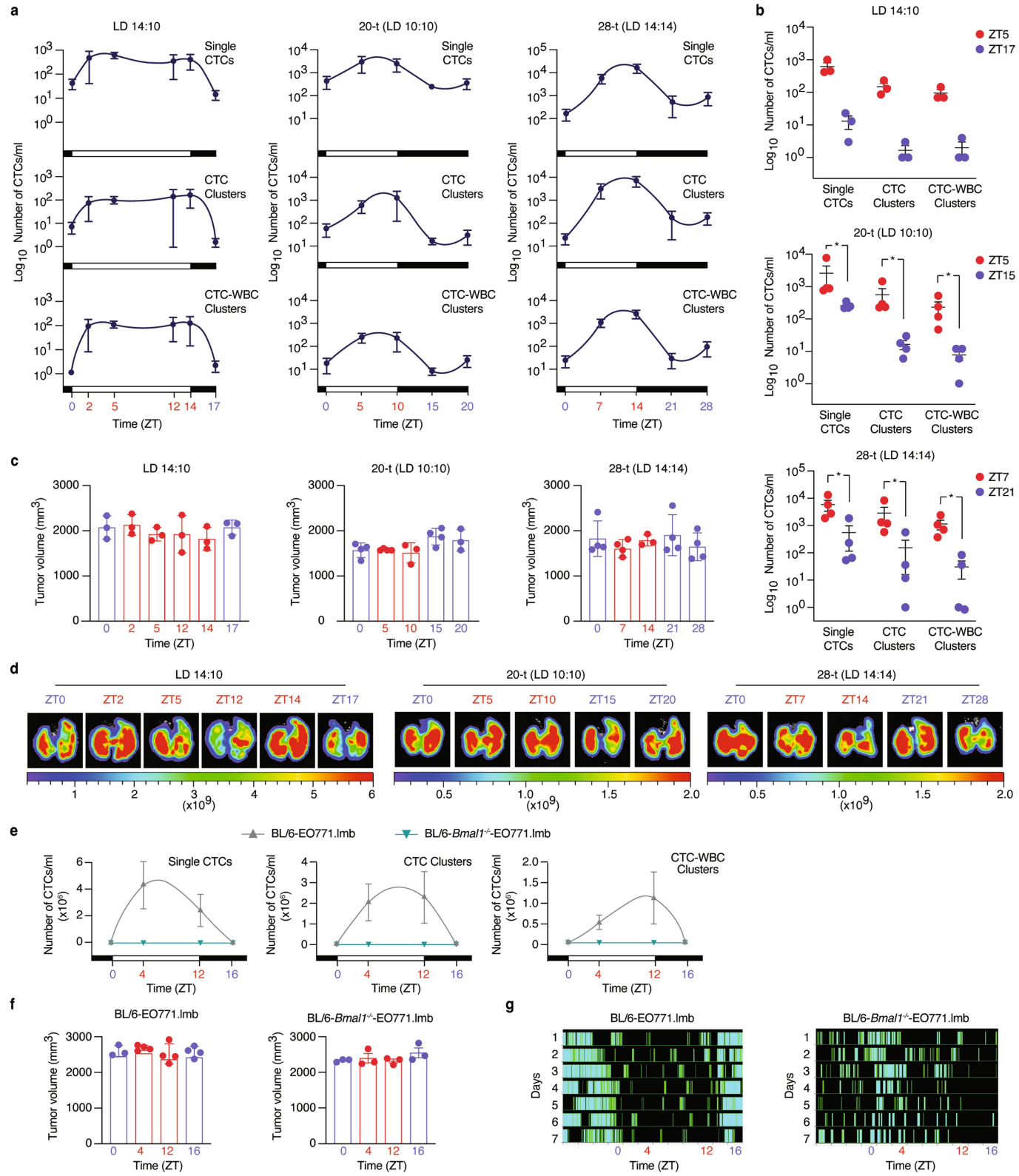

Extended Data Fig. 4 | See next page for caption.

Extended Data Fig. 4 | Light exposure impacts CTC intravasation. a, Time kinetic analysis showing mean CTC counts (single CTCs, CTC clusters and CTC-WBC clusters) in the NSG-LM2 mice kept in altered light-dark (LD) cycles (LD 14:10, $n = 3$; LD 10:10, $n = 4$, except ZT10 and ZT20 where $n = 3$; LD 14:14, $n = 4$, except ZT14 where $n = 3$). **b**, Scatter dot plots showing the distribution of the number of single CTCs, CTC clusters and CTC-WBC clusters isolated from NSG-LM2 mice that were kept in altered light cycles (LD 14:10, $n = 3$; LD 10:10, $n = 4$; LD 14:14, $n = 4$; $P = 0.0286$ for all). * $P < 0.05$ by two-sided Mann-Whitney test. **c**, Plots showing the size of primary tumors dissected from NSG-LM2 mice shown in "a". **d**, Representative bioluminescence images of lungs from NSG-LM2 mice shown in "a". **e**, Graphs showing time kinetic analysis of CTC counts (single CTCs, CTC clusters and CTC-WBC clusters) in the BL/6-EO771.lmb (ZT4, ZT12, ZT16 $n = 4$; ZT0 $n = 3$) and BL/6-*Bmal1*$^{-/-}$-EO771.lmb ($n = 3$) breast cancer mouse models collected via tumor draining vessel (TDV) over a 24-h time period. **f**, Plots showing the size of the primary tumors dissected from BL/6-EO771.lmb and BL/6-*Bmal1*$^{-/-}$-EO771.lmb mice shown in Fig. 1d. **g**, Plotted actograms showing the running activity of the BL/6-EO771.lmb and BL/6-*Bmal1*$^{-/-}$-EO771.lmb mice with dark and light areas representing low and high activity, respectively. For all panels, data are presented as mean ± s.e.m. n represents the number of biologically independent mice.

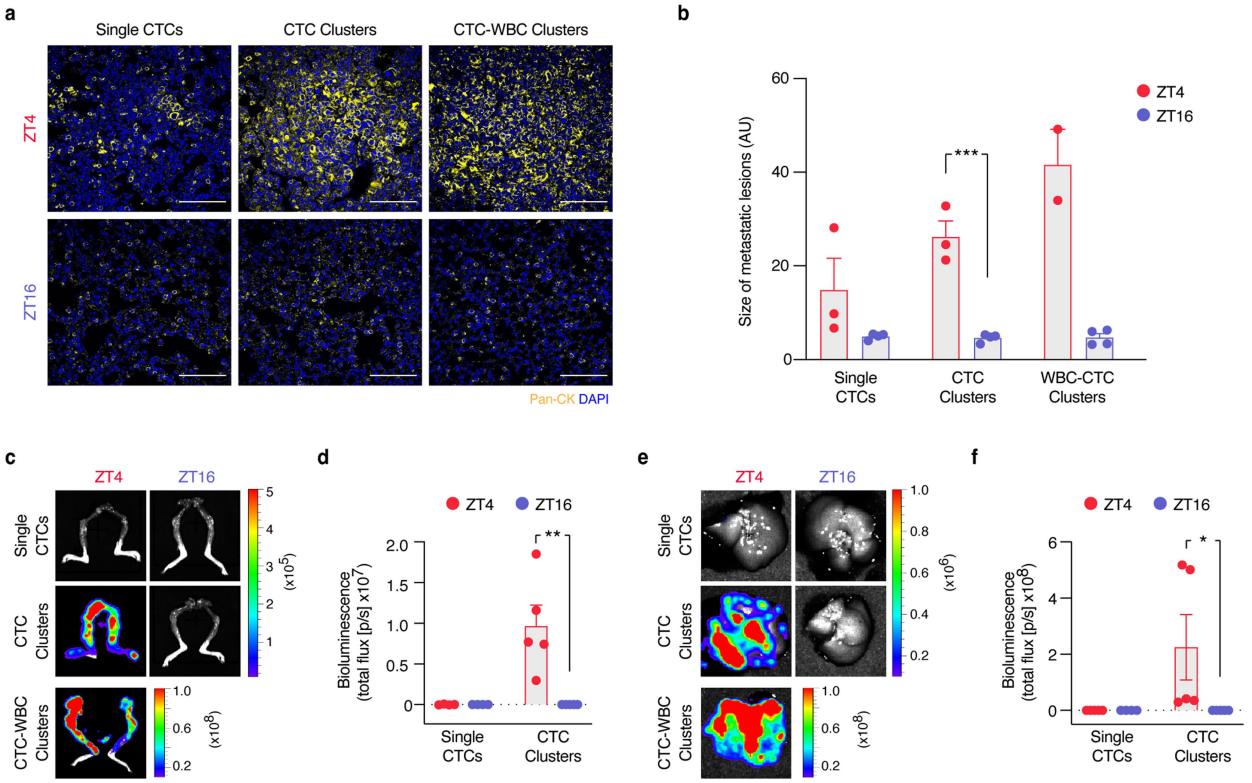

Extended Data Fig. 5 | Rest-phase CTCs have increased metastatic potential. a, Representative immunofluorescence images for Pan-CK in lungs of mice injected with single CTCs, CTC clusters and CTC-WBC clusters collected at ZT4 or ZT16 from NSG-LM2 mice (ZT4 $n = 3$ except CTC-WBC clusters $n = 2$; ZT16 $n = 4$ for all). Scale bar = 100 µm. **b**, Plot showing the size of the metastatic lesions detected in the lungs of mice injected with single CTCs, CTC clusters or CTC-WBC clusters collected at ZT4 or ZT16 of NSG-LM2 mice (ZT4 $n = 3$ except CTC-WBC clusters $n = 2$; ZT16 $n = 4$ for all; $P = 0.0007$). **c**, Representative bioluminescence images of bones from mice injected with single CTCs, CTC clusters or CTC-WBC clusters collected at ZT4 or ZT16 from NSG-CDX-BR16 mice. Mice were not injected with CTC-WBC clusters collected during the active phase, due to their rarity. **d**, Plot showing normalized bioluminescence signal obtained from bones of mice shown in panel "c" (single CTCs $n = 4$; CTC clusters $n = 5$; $P = 0.006$). **e**, Representative bioluminescence images of livers from mice injected with single CTCs or CTC clusters, collected at ZT4 or ZT16 from NSG-CDX-BR16 mice. Mice were not injected with CTC-WBC clusters collected during the active phase, due to their rarity. **f**, Plot showing normalized bioluminescence signal obtained from liver of mice shown in panel "e" ($n = 5$ except single CTCs collected at ZT16 where $n = 4$; $P = 0.0301$). For all panels, data are presented as mean ± s.e.m.; unpaired two-sided t-test * $P < 0.05$, ** $P < 0.01$, *** $P < 0.001$. n represents the number of biologically independent mice.

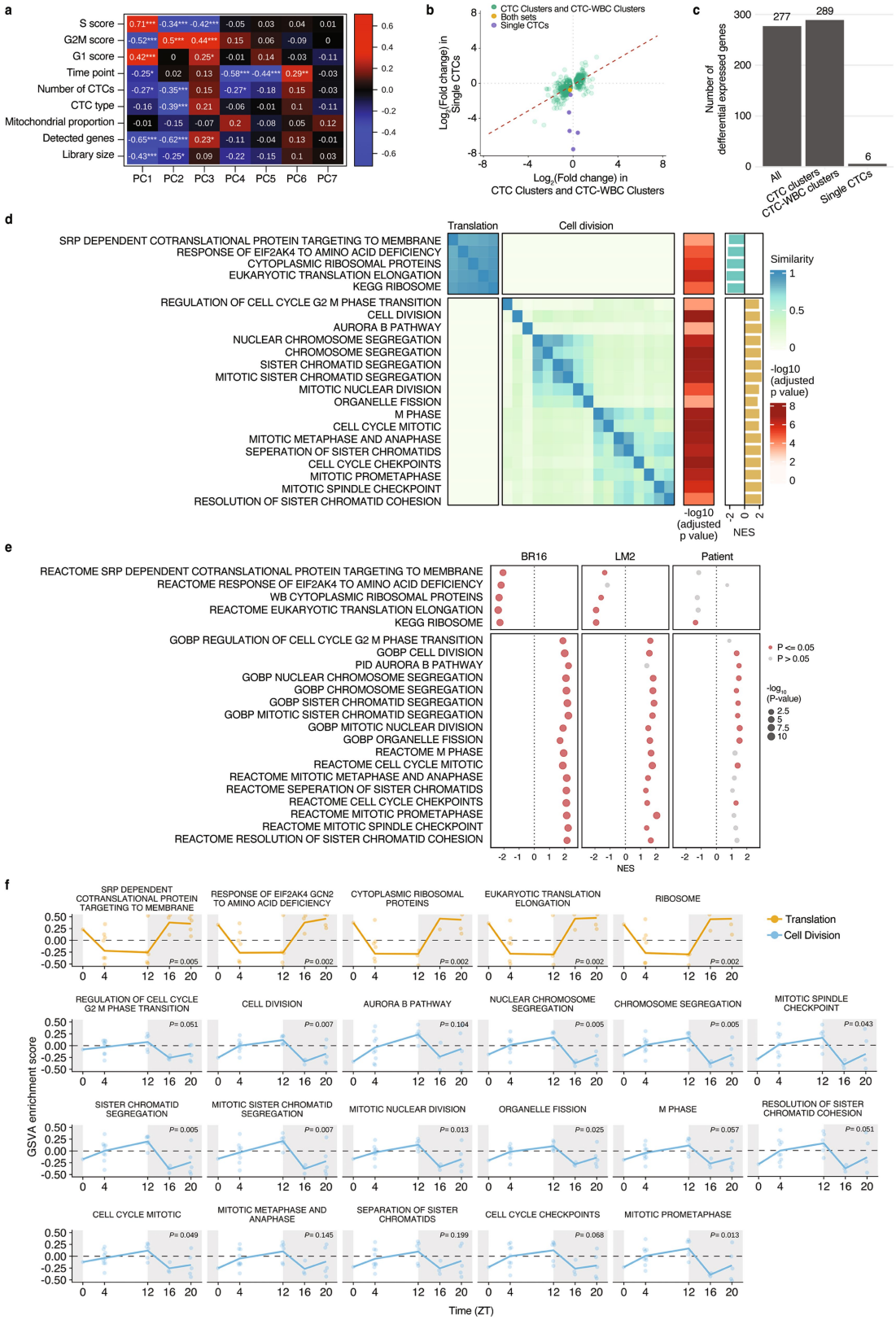

Extended Data Fig. 6 | See next page for caption.

Extended Data Fig. 6 | Time point of CTC isolation is the main determinant of gene expression heterogeneity in CTCs. a, Heatmap showing the Pearson's correlation coefficient of PC1-7 eigenvectors from gene expression with technical and biological variables in BR16-CDX CTCs. *P* values by two-sided Pearson's correlation test (*$P < 0.01$, **$P < 0.001$, ***$P < 0.0001$). **b**, Scatter plot showing the correlation of the fold-change between active and rest phase in single CTC (Y-axis) versus CTC clusters and CTC-WBC (X-axis), using genes with *FDR* ≤ 0.05 in any of the two sets (two-sided Pearson's correlation coefficient 0.57, *P* value ≤ 2.22e-16). Points are colored according to the dataset where they were found with a *FDR* ≤ 0.05 (both, single CTC or CTC clusters and CTC-WBC clusters). The dashed *red* line represents the linear regression line using all the points in the plot. **c**, Bar plot showing the number of differentially expressed genes (absolute $\log_2$ fold change ≥ 0.5 and *FDR* ≤ 0.05) using all the samples ('All'), using clustered CTCs (CTC clusters and CTC-WBC clusters) and using single CTCs. **d**, Heatmap showing the pair-wise similarity matrix of enriched gene sets (gene set enrichment analysis (GSEA) adjusted *P* value ≤ 0.001) using differential expression between CTCs of rest and active phase from NSG-CDX-BR16 mice. Heatmap colors represent the Jaccard similarity coefficient using the set of core genes in each gene set. The heatmap on the *right* represents the GSEA adjusted *P* value. **e**, Plots comparing the normalized enrichment score (NES) and adjusted *P* value (dot size) obtained using GSEA for gene sets shown in "d". Gene sets with an adjusted *P* value ≤ 0.05 in each sample set are highlighted in *red*. **f**, GSVA score for translation (*yellow*, $n = 5$) and cell division (*blue*, $n = 17$) gene sets in CTCs obtained from the NSG-LM2 time-kinetics experiment. *Yellow* and *blue* lines represent the average at each time point. Individual points represent the enrichment score for each CTC sample. The *white* and *grey* backgrounds represent environmental light (rest period) and dark conditions (active period), respectively. Adjusted F-test *P* values as obtained from limma are shown for each individual gene set.

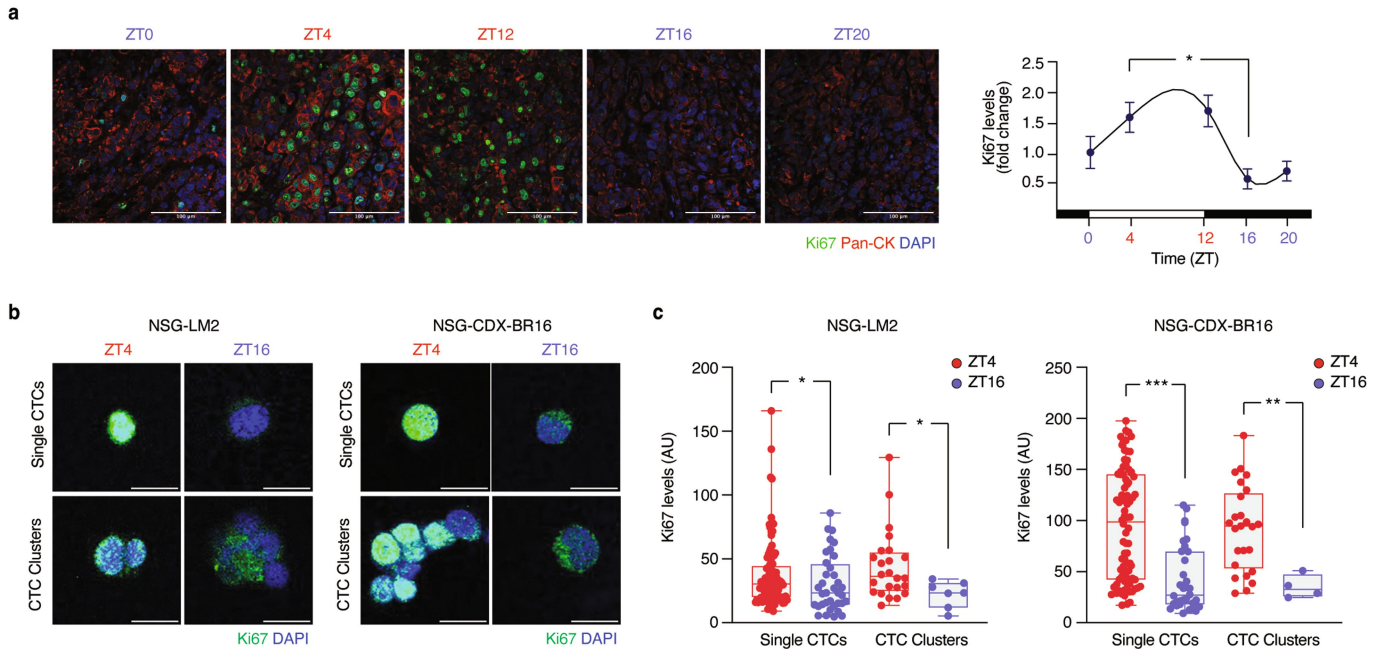

Extended Data Fig. 7 | The proliferation status of primary tumours changes in a circadian rhythm dependent manner. a, Representative immunofluorescence images of Ki67 and Pan-CK in primary tumors from NSG-CDX-BR16 mice, dissected at different timepoints (ZT0, ZT4, ZT12, ZT16, ZT20) over a 24-h time period (ZT4, ZT12, ZT16 $n = 3$; ZT0, ZT20 $n = 2$; $P = 0.0270$; scale bar = 100 µm) (*left*). The plot shows the intensity of Ki67 in tumors of NSG-CDX-BR16 mice during different timepoints (*right*). Data are presented as mean ± s.e.m.; unpaired two-sided *t*-test * $P < 0.05$. **b**, Representative immunofluorescence images of Ki67 in CTCs collected at ZT4 and ZT16 from NSG-LM2 and NSG-CDX-BR16 mice. Scale bar = 10 µm. **c**, Plots showing the distribution of Ki67 intensity in single CTCs (NSG-LM2 $P = 0.0495$; NSG-CDX-BR16 $P = 0.0001$) and CTC clusters (NSG-LM2 $P = 0.0223$; NSG-CDX-BR16 $P = 0.0045$) collected at ZT4 and ZT16 from NSG-LM2 and NSG-CDX-BR16 mice ($n = 3$). Box center lines in the box represent the median; limits represent first and third quartile; extremes of the whisker lines represent the minimum and maximum observed values. * $P < 0.05$, ** $P < 0.01$, *** $P < 0.001$ by two-sided Mann-Whitney test. For all panels, *n* represents the number of biologically independent mice.

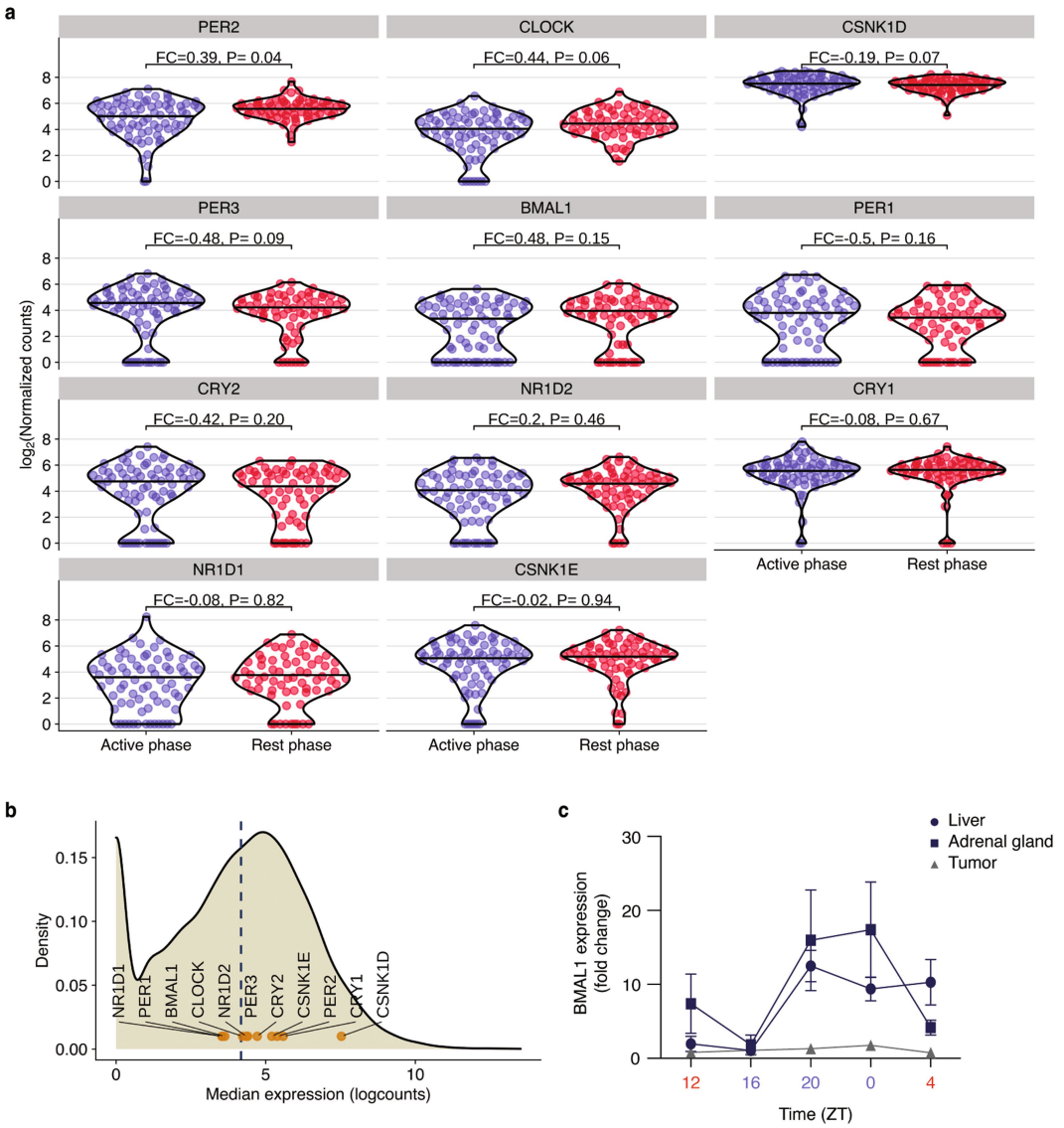

Extended Data Fig. 8 | Breast cancer derived CTCs lack a functional circadian clock. a, Plot showing the expression distribution of core circadian genes in CTCs from NSG-CDX-BR16 mice. The fold change (FC, in $\log_2$ scale) and adjusted *P* value from the global differential expression analysis are shown for each gene. **b**, Density plot showing the distribution of the average expression ($\log_2$ counts per million) of genes in CTCs from NSG-CDX-BR16 mice. Core circadian genes are labeled in the X-axis. **c**, qPCR for *Bmal1* expression in the liver, adrenal glands and primary tumor of NSG-LM2 mice ($n = 3$ for all the time points of the adreanal glands; $n = 3$ for all the time points of the liver and tumor, except ZT4 and ZT20 where $n = 4$). Data are relative to the time point with the lowest expression levels of *Bmal1* (ZT16; set as 1) and are presented as mean ± s.e.m. *n* represents the number of biologically independent mice.

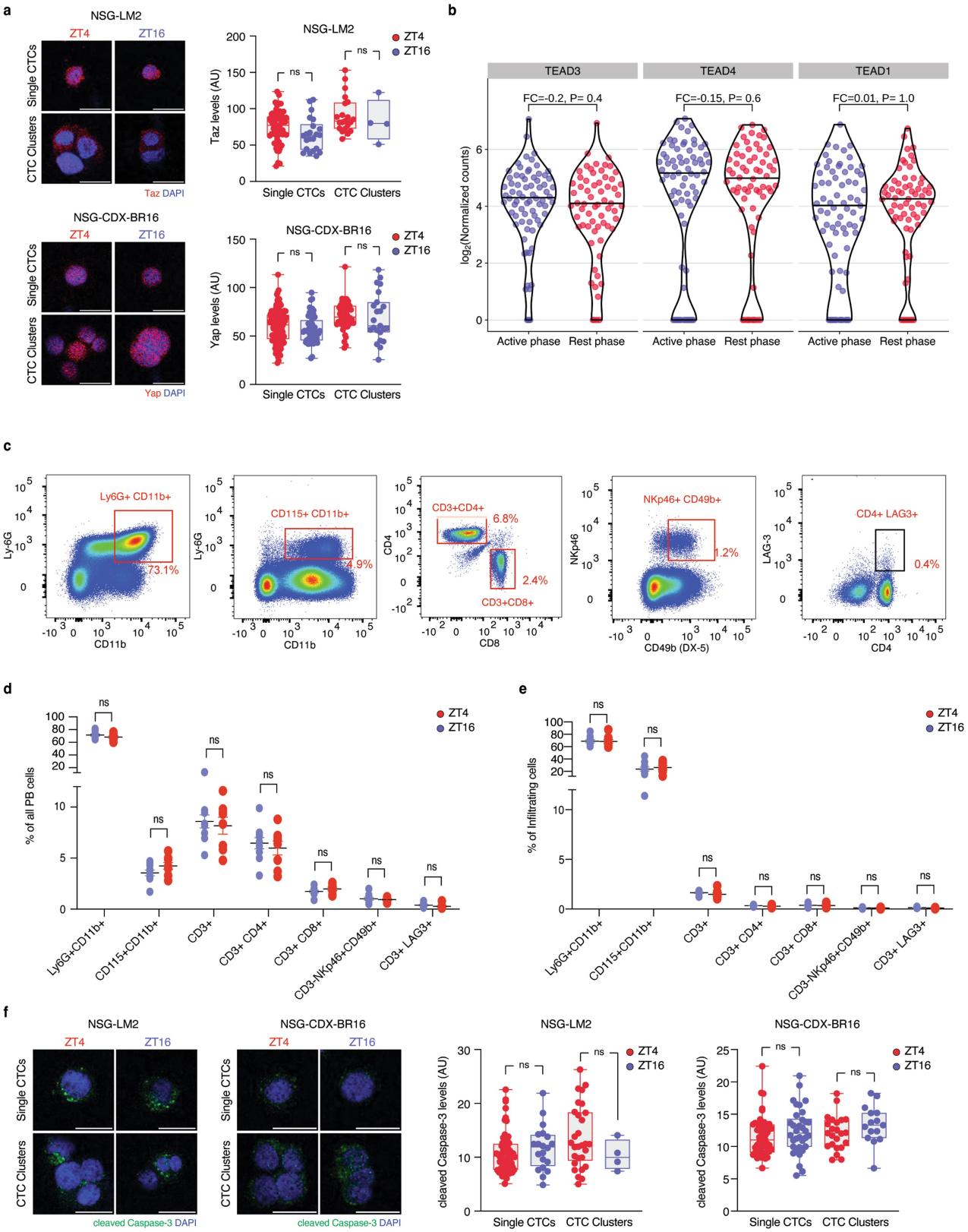

Extended Data Fig. 9 | See next page for caption.

Extended Data Fig. 9 | Assessment of interestial pressure, immunosurveillance and apoptosis in CTCs at different timepoints of the circadian rhythm. a, Representative immunofluorescence images of Taz and Yap in CTCs collected at ZT4 and ZT16 from NSG-LM2 and NSG-CDX-BR16 mice. Plots showing the distribution of Taz and Yap intensity in CTCs shown in the same panel ($n = 3$). Scale bar = 10 µm. **b**, Plot showing the expression distribution of TEAD genes in CTCs from NSG-CDX-BR16 mice. The fold change (FC, in $\log_2$ scale) and adjusted *P* value from the global differential expression analysis are shown for each gene. **c**, Gating strategy to determine the frequency of the indicated cell populations in panels "d" and "e". The percentage values refer to the parental population considered in each panel. **d**, Plot showing the frequency of white blood cells (WBCs) from peripheral blood (PB) isolated during the rest ($n = 8$) or active phase ($n = 10$) from BALB/c-4T1 mice. **e**, Plot showing the frequency of tumor-infiltrated WBCs isolated during the rest ($n = 8$) or active phase ($n = 10$) from BALB/c-4T1 mice. **f**, Representative immunofluorescence images of cleaved caspase-3 in CTCs collected at ZT4 and ZT16 from the NSG-LM2 and NSG-CDX-BR16 mice. Plots showing the distribution of cleaved caspase-3 intensity in CTCs shown in the same panel ($n = 3$). Scale bar = 10 µm. For panels "a" and "f", center lines in the box represent the median; box limits represent first and third quartile; extremes of the whisker lines represent the minimum and maximum observed values. ns: non statistically significant by two-sided Mann-Whitney test. For panels "d" and "e", data are presented as mean ± s.e.m.; ns: non statistically significant by unpaired two sided *t*-test. For all panels, *n* represents the number of biologically independent mice.

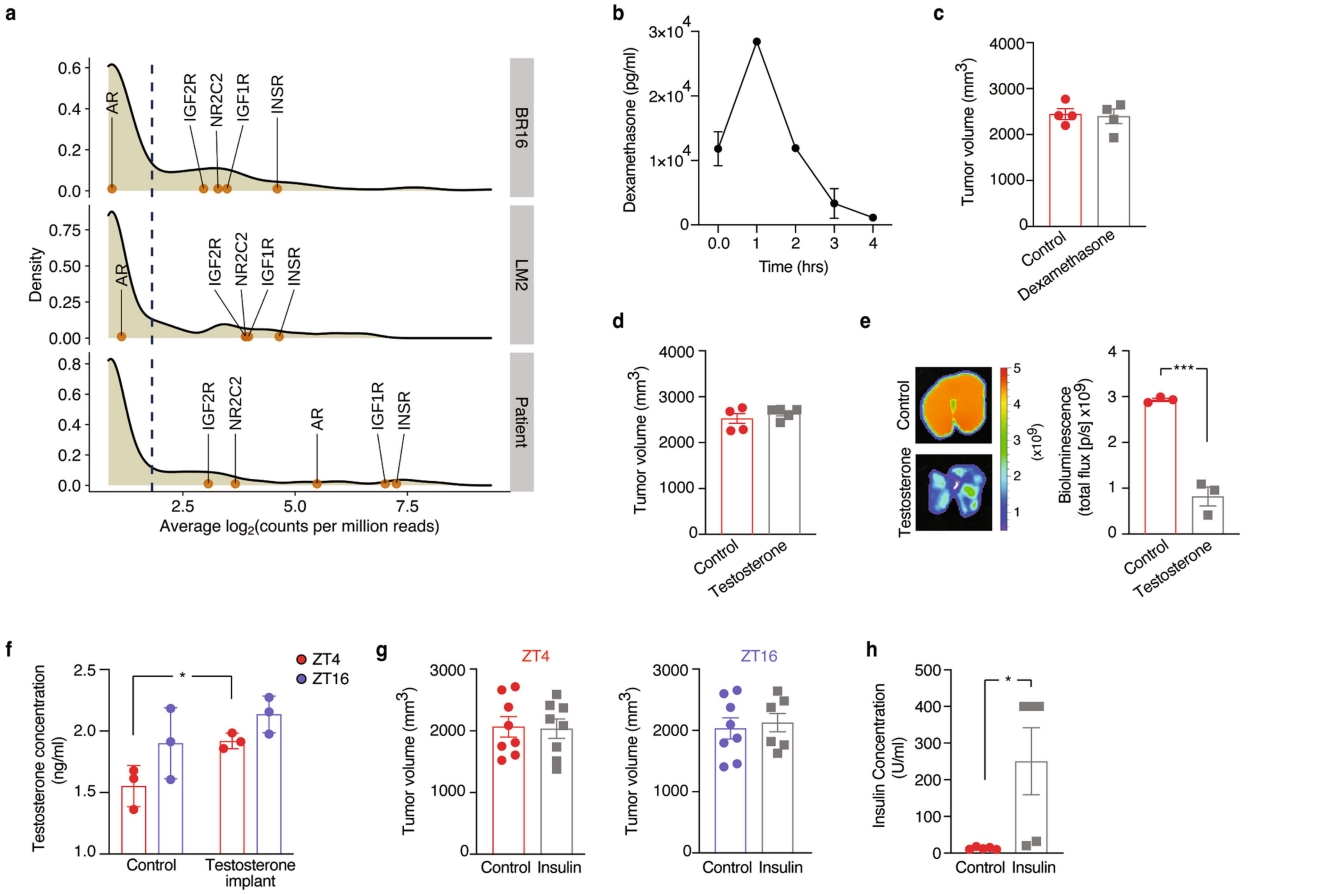

Extended Data Fig. 10 | Expression of receptors activated by circadian rhythm regulated ligands. a, Density plots showing the distribution of the average expression (log_2 counts per million) of genes encoding for receptors of circadian-regulated hormones, growth factors or molecules in CTCs from NSG-CDX-BR16 mice, NSG-LM2 mice and patients with breast cancer. Genes for the glucocorticoid receptor, androgen receptor and insulin receptor are labeled in the X-axis. **b**, Time kinetic plot showing the pharmacokinetic profile of dexamethasone-treated mice ($n = 2$). **c**, Plots showing the size of the primary tumors dissected from dexamethasone-treated or control NSG-LM2 mice ($n = 4$). **d**, Plots showing the size of the primary tumors dissected from testosterone-treated ($n = 5$) or control NSG-LM2 mice ($n = 4$). **e**, Representative bioluminescence images of lungs from untreated or testosterone-treated NSG-LM2 mice (*left*). Plot showing normalized bioluminescence signal obtained from lungs of testosterone-treated or control NSG-LM2 mice ($n = 3$; $P = 0.0005$). **f**, Plot showing plasma concentration of testosterone in control and testosterone-treated mice ($n = 3$; $P = 0.0237$). **g**, Plots showing the primary tumors dissected from control or insulin-treated mice at ZT4 and ZT16 ($n = 8$, except insulin-treated mice at ZT16 where $n = 6$.). **h**, Plot showing plasma concentration of insulin in control and insulin treated mice ($n = 5$; $P = 0.0321$). For all panels, data are presented as mean ± s.e.m.; For panels "e", "f" and "h", * $P < 0.05$, *** $P < 0.001$ by unpaired two sided *t*-test. For all panels, *n* represents the number of biologically independent mice.

nature portfolio

Corresponding author(s): Aceto Nicola

Last updated by author(s): Apr 25, 2022

Reporting Summary

Nature Portfolio wishes to improve the reproducibility of the work that we publish. This form provides structure for consistency and transparency in reporting. For further information on Nature Portfolio policies, see our Editorial Policies and the Editorial Policy Checklist.

Statistics

For all statistical analyses, confirm that the following items are present in the figure legend, table legend, main text, or Methods section.

n/a	Confirmed
☐	☒ The exact sample size (*n*) for each experimental group/condition, given as a discrete number and unit of measurement
☐	☒ A statement on whether measurements were taken from distinct samples or whether the same sample was measured repeatedly
☐	☒ The statistical test(s) used AND whether they are one- or two-sided *Only common tests should be described solely by name; describe more complex techniques in the Methods section.*
☒	☐ A description of all covariates tested
☐	☒ A description of any assumptions or corrections, such as tests of normality and adjustment for multiple comparisons
☐	☒ A full description of the statistical parameters including central tendency (e.g. means) or other basic estimates (e.g. regression coefficient) AND variation (e.g. standard deviation) or associated estimates of uncertainty (e.g. confidence intervals)
☐	☒ For null hypothesis testing, the test statistic (e.g. *F*, *t*, *r*) with confidence intervals, effect sizes, degrees of freedom and *P* value noted *Give P values as exact values whenever suitable.*
☒	☐ For Bayesian analysis, information on the choice of priors and Markov chain Monte Carlo settings
☒	☐ For hierarchical and complex designs, identification of the appropriate level for tests and full reporting of outcomes
☐	☒ Estimates of effect sizes (e.g. Cohen's *d*, Pearson's *r*), indicating how they were calculated

Our web collection on statistics for biologists contains articles on many of the points above.

Software and code

Policy information about availability of computer code

Data collection	No software or code was used to collect data.
Data analysis	Confocal images were analyzed by the Fiji image processing software (2.1.0/1.53c). Metastasis analysis was performed by the IVIS Bioluminescence System (4.5.4). FACS samples were analysed with FlowJo (Tree Star). Data analysis, statistical testing and visualization were conducted in Graphpad Prism (v.9.1.1), R (version 4.1.0; R Foundation for Statistical Computing) and bioconductor (v.3.13). For RNA sequencing data quality control Trim Galore! (v0.6.5), FastQC (v0.11.4), FastQ Screen (v0.11.4), RSeQC (v.2.6.4) and MultiQC (v1.7) were used. For RNA sequencing alignment pipeline we used STAR (v.2.7.3a), Disambiguate (v1.0.0), Samtools (v1.10), featureCounts (v.2.0.1). For quality control, analysis, and visualization of processed RNA-seq data we used R/Bioconductor packages scater (v1.20.1), scran (v1.20.1), edgeR (v3.34.1), clusterProfiler (v4.0.5), fgsea (v1.18.0), GSVA (v 1.40.1), limma (v3.48.3), ComplexHeatmap (v 2.8.0) and PCAtools (v 2.4.0). Code for RNA sequencing data analysis is available at https://github.com/TheAcetoLab/diamantopoulou-ctc-dynamics and archived at Zenodo (https://doi.org/10.5281/zenodo.6484917). Description of how to reproduce the analysis workflow showing code and R packages version numbers is available from https://theacetolab.github.io/diamantopoulou-ctc-dynamics

For manuscripts utilizing custom algorithms or software that are central to the research but not yet described in published literature, software must be made available to editors and reviewers. We strongly encourage code deposition in a community repository (e.g. GitHub). See the Nature Portfolio guidelines for submitting code & software for further information.

Data

Policy information about availability of data

All manuscripts must include a data availability statement. This statement should provide the following information, where applicable:

- Accession codes, unique identifiers, or web links for publicly available datasets
- A description of any restrictions on data availability
- For clinical datasets or third party data, please ensure that the statement adheres to our policy

Raw RNA sequencing data have been deposited in the Gene Expression Omnibus (GEO, NCBI; accession number GSE180097). Processed RNA sequencing data and other large data sets required for reproducibility are available from the Zenodo data repository (https://doi.org/10.5281/zenodo.6358987).
Human reference genome (GRCh38), mouse reference genome (GRCm38), human gene annotation (release 35) and mouse gene annotation (release M25) were downloaded from GENCODE (https://www.gencodegenes.org). Gene sets were downloaded from the Molecular Signatures Database (MsigDB, v7.4, http://www.gsea-msigdb.org/gsea/msigdb/collections.jsp). All data are available from the corresponding author upon reasonable request.

Field-specific reporting

Please select the one below that is the best fit for your research. If you are not sure, read the appropriate sections before making your selection.

☒ Life sciences ☐ Behavioural & social sciences ☐ Ecological, evolutionary & environmental sciences

For a reference copy of the document with all sections, see nature.com/documents/nr-reporting-summary-flat.pdf

Life sciences study design

All studies must disclose on these points even when the disclosure is negative.

Sample size	For the animal studies, sample size calculations were not predetermined, but number of animals were chosen to comply with the 3R principles. For the bioinformatic analysis, no statistical method was used to pre-determine the sample size for RNA-seq experiments. Sample size was determined based on our previous experience with CTC isolation from NSG-LM2 and NSG-CDX-BR16 models. For patient data, the sample size was determined by the availability of CTCs in circulation.
Data exclusions	Animals that were active during the rest phase or they were sleeping during the active phase were not analysed.
Replication	The effect of the circadian rhythm on the intravasation of CTCs was confirmed in different mouse models (NSG-LM2, NSG-CDX-BR16, NSG-4T1, BALB/c-4T1, BL/6-EO771.lmb and BL/6-Bmal1-/--E0771.lmb) and in independent experimental replicates (NSG-LM2 n=8; NSG-CDX-BR16 n=3; NSG-4T1 n=2; BALB/c-4T1 n=1; IBL/6-EO771.lmb n=2; BL/6-Bmal1-/--E0771.lmb n=2; n=number of independent experimental replicates). In all experiments and replicates the effect of the circadian rhythm on the intravasation of CTCs was the same. The metastatic potential of the rest or active phase collected CTCs was tested in two different mouse models (NSG-LM2, NSG-CDX-BR16) and the results were reproducible. We performed 3 independent experimental replicates for the NSG-LM2 model and 1 independent experimental replicate for the NSG-CDX-BR16 due to long time required for the tumour formation (>1 year). Results were confirmed in 30 breast cancer patients with different clinical features (Supplementary Table 1). Samples from four additional early stage breast cancer patients were analysed, but no CTCs were found during neither the rest nor active phase, even though the experimental procedure was carried out successfully. 138 CTCs from the NSG-CDX-BR16 model and 108 CTCs from the NSG-LM2 model, collected from three mice per condition, were used for the bioinformatic analysis. Cell division and translational gene expression signatures were significantly enriched in all the experiments and therefore these results are highly reproducible.
Randomization	All mice were randomized before the start of each experiment and randomly allocated in different groups before the start of each drug treatment. All patients participants were hospitalized women with progressive breast cancer that had no treatment or were temporarily off-treatment. Participants were grouped into an early (no metastasis detected) or late group (metastasis detected). We didn't control for covariates, as we analysed differences on CTC numbers at two different time points of the same patient and we didn't perform any comparison between the two groups.
Blinding	Both patients and mouse samples were encrypted. The investigators were not blinded during this study, as checking the activity state of each mouse was a prerequisite for excluding samples from the study. Furthermore, blinding was not possible as many analyses were performed by the person in charge of sampling. Blinding during confocal imaging analysis was not feasible as the differences between samples were visually apparent. During sequencing data processing and quality control, the person in charge was blinded to sample condition. Posterior analysis such as differential expression, required sample re-identification.

Reporting for specific materials, systems and methods

We require information from authors about some types of materials, experimental systems and methods used in many studies. Here, indicate whether each material, system or method listed is relevant to your study. If you are not sure if a list item applies to your research, read the appropriate section before selecting a response.

Materials & experimental systems

n/a	Involved in the study
☐	☒ Antibodies
☐	☒ Eukaryotic cell lines
☒	☐ Palaeontology and archaeology
☐	☒ Animals and other organisms
☐	☒ Human research participants
☒	☐ Clinical data
☒	☐ Dual use research of concern

Methods

n/a	Involved in the study
☒	☐ ChIP-seq
☐	☒ Flow cytometry
☒	☐ MRI-based neuroimaging

Antibodies

Antibodies used

In this study we used the following primary antibodies: pan-CK (1:65; GeneTex, GTX27753), Ki67 (1:250; Abcam, ab15580), GFP (D5.1; 1:200; Cell Signaling Technology, 2956), mCherry (16D7; 1:300: Invitrogen, M11217), TAZ (1:100; BD Biosciences, 560235), YAP (D8H1X; 1:1000; Cell Signaling Technology, 14074), cleaved-caspase3 (5A1E; 1:100; Cell Signaling Technology, 9664), EpCAM-AF488 (Cell Signaling Technology, CST5198), HER2-AF488 (BioLegend, 324410), EGFR-FITC (GeneTex, GTX11400), CD45-BV605 (BioLegend, 304042), CD90.1 (OX-7 clone, BioLegend, 202508), Alexa Fluor® 594 anti-mouse Ly-6G (1A8 clone, BioLegend, 127602), Alexa Fluor® 594 anti-mouse CSF-1R/CD115 (AFS98 clone, BioLegend, 135520), APC/Cyanine7 anti-CD11b Antibody (M1/70 clone, BioLegend, 101226), Brilliant Violet 421™ anti-mouse CD3 (17A2 clone, BioLegend, 100228), PE anti-mouse NKp46/CD335 (29A1.4 clone, BioLegend, 137647), Alexa Fluor® 647 anti-mouse CD49b (DX5 clone, BioLegend, 103511), Alexa Fluor® 488 anti-mouse CD8a (53-6.7 clone, BioLegend, 100723), Brilliant Violet 510™ anti-mouse CD4 (GK1.5 clone, BioLegend, 100449) and PE anti-mouse CD223/LAG-3 (C9B7W clone, BioLegend, 125224).

Validation

Based on key features provided by Abcam (https://www.abcam.com/ki67-antibody-ab15580.html), the Ki67 antibody used in this study is knockout validated and is suitable for IF/ICC/IHC in human and mouse samples. Our data (staining of CTCs collected from the NSG-LM2 and NSG-CDX-BR16 model during the rest or active phase) show a clear and strong difference at the levels of Ki67, confirming its specificity. The pan-CK antibody was previously validated from our lab (Scheidmann et al., Cancer Res, 2022), and additionally our data show that this antibody, used in an optimal concentration, strongly recognizes human tumours formed in lungs of mice. YAP and TAZ antibodies were previously validated (Diamantopoulou et al., Cancer Cell, 2017). We validated the cleaved-caspase3 that was suitable for IHC/IF, by testing different dilutions in samples from mouse spleens that are strongly apoptotic, confirming its activity as provided by its manufacturer (https://www.cellsignal.com/products/primary-antibodies/cleaved-caspase-3-asp175-5a1e-rabbit-mab/9664). The rest of the antibodies were previously validated by our lab (Szczerba et al., Nature, 2019).

Eukaryotic cell lines

Policy information about cell lines

Cell line source(s)

Human CTC-derived BR16 cells were generated from a patient with hormone receptor-positive breast cancer at the University Hospital Basel. MDA-MB-231 LM2 human breast cancer cells were obtained from J. Massagué, Memorial Sloan Kettering Cancer Center. E0771.lmb mouse breast cancer cells were originally generated and obtained from Robin Anderson, Olivia Newton-John Cancer Research Institute. 4T1 mouse breast cancer cells were purchased from ATCC.

Authentication

Authentication is not applicable for the human CTC-derived BR16 athe MDA-MB-231 LM2 human breast cancer cells variant, as well as the E0771.lmb mouse breast cancer variant. 4T1 mouse breast cancer cells were authenticated by Multiplexion GmbH.

Mycoplasma contamination

All cell lines were tested by Multiplexion GmbH or IDEXX BioAnalytics and were negative for mycoplasma.

Commonly misidentified lines
(See ICLAC register)

No misindentified lines were used in this study.

Animals and other organisms

Policy information about studies involving animals; ARRIVE guidelines recommended for reporting animal research

Laboratory animals

8 weeks-old NSG (NOD-scid-Il2rgnull) and BALB/c female mice were purchased from the Jackson Laboratory or Janvier Labs, respectively. 8 weeks-old C57BL/6J female mice were purchased from The Jackson Laboratory. Bmal1 knockout mice (C57BL/6J background) were purchased and genotyped from the The Jackson Laboratory. All animals were maintained at 24-26°C with 55% humidity.

Wild animals

This study did not involve wild animals.

Field-collected samples

This study did not involve samples collected form the field.

Ethics oversight

All mouse experiments were carried out according to institutional and cantonal guidelines (approved mouse protocol #3053, cantonal veterinary office of Basel-City and approved mouse protocol #33688, cantonal veterinary office of Zurich).

Note that full information on the approval of the study protocol must also be provided in the manuscript.

Human research participants

Policy information about studies involving human research participants

Population characteristics	In this study, we used hospitalized women with progressive breast cancer that were either temporarily off-treatment (patients with stage IV) or before operation (patients with stage I-III) at the time of blood sampling. Patients were at different age (Suppl Table 1).
Recruitment	Clinicians recruited hospitalized women with progressive breast cancer. As the number of CTCs is affected by treatment therapies, we selected patients that had no treatment or they were temporarily off-treatment. We didn't apply any other selection criteria. Clinicians explained in details about the project workflow, risks, patients' rights and how the donated samples were encrypted. Patients were informed about the impact that our study could have on future anti-cancer therapies. Clinicians replied to all the questions that patients raised. Patients were given the time to think and decide in free will.
Ethics oversight	This study took place at the University Hospital Basel under the Clinical Research Protocol (#2020-00014) approved by the Swiss authorities (EKNZ, Ethics Committee northwest/central Switzerland) and in compliance with the Declaration of Helsinki.

Note that full information on the approval of the study protocol must also be provided in the manuscript.

Flow Cytometry

Plots

Confirm that:

☒ The axis labels state the marker and fluorochrome used (e.g. CD4-FITC).

☒ The axis scales are clearly visible. Include numbers along axes only for bottom left plot of group (a 'group' is an analysis of identical markers).

☒ All plots are contour plots with outliers or pseudocolor plots.

☒ A numerical value for number of cells or percentage (with statistics) is provided.

Methodology

Sample preparation	Mouse tumours were minced in fragments and enzymatically digested for 15 minutes with 2 mg/ml type IV Collagenase plus 50 U/ml bovine DNase. The digested tumours were mechanically dissociated in C-tubes using a GentleMACS device (Miltenyi), then subjected to red blood cell lysis using ACK Buffer (Lonza) and immediately stained. Whole mouse blood was pelleted and red blood cells were lysed using ACK Buffer and immediately stained. For immunostaining, cells were blocked in a 2% FCS solution containing 2 mM Ethylenediaminetetraacetic acid (EDTA) and FcR blocking reagent (Miltenyi).
Instrument	All samples were processed on an LSR Fortessa device (BD).
Software	All samples were analysed with FlowJo (Tree Star).
Cell population abundance	No sorting was performed.
Gating strategy	Control stains (unstained and single stained cells) were used to set gates. All samples were first FSC-A and SSC-A gated or FSC-H and SSC-H gated depending on the origin (tumours or peripheral blood). Gating for total leukocytes was conducted in peripheral blood samples based on their typical pattern, while gating for stromal cells was conducted on CD90.1+ tumours based on negativity for the CD90.1 marker. Subsequent relevant gating was conducted as shown in the gating strategy exemplifying figure.

☒ Tick this box to confirm that a figure exemplifying the gating strategy is provided in the Supplementary Information.